SPOP mutation confers sensitivity to AR-targeted therapy in prostate cancer by reshaping the androgen-driven chromatin landscape

Ivana Grbesa[1,2], Michael A. Augello[1,2,], Deli Liu[1,2,3], Dylan R. McNally[4,5,6], Christopher D. Gaffney[1], Dennis Huang[1,2], Kevin Lin[2], Ramy Goueli[1], Brian D. Robinson[5,7], Francesca Khani[5,7], Lesa D. Deonarine[1,2], Mirjam Blattner[2,7], Olivier Elemento[3,5,7], Elai Davicioni[8], Andrea Sboner[2,3,5,7], Christopher E. Barbieri[1,2,5*]†

[1]Department of Urology, Weill Cornell Medicine, New York, NY 10065, USA.

[2]Sandra and Edward Meyer Cancer Center, Weill Cornell Medicine, New York, NY 10065, USA.

[3]The HRH Prince Alwaleed Bin Talal Bin Abdulaziz Alsaud Institute for Computational Biomedicine, Weill Cornell Medicine, New York, NY 10065, USA.

[4]Department of Physiology and Biophysics, Weill Cornell Medicine, New York, NY 10065, USA.

[5]Caryl and Israel Englander Institute for Precision Medicine, Weill Cornell Medicine, New York, NY 10065, USA.

[6]Department of Medicine and Weill Cornell Cancer Center, Weill Cornell Medicine, New York, NY 10021, USA.

[7]Department of Pathology and Laboratory Medicine, Weill Cornell Medicine, New York, NY 10065, USA.

[8]GenomeDx Bioscience, Vancouver, British Columbia, BC V6B 4X2, Canada.

*To whom correspondence should be addressed: chb9074@med.cornell.edu

†Lead Contact

Keywords: prostate cancer, androgen receptor, FOXA1, organoids, androgen-deprivation therapy, epigenomic landscape

Additional Information

Financial support

This work was funded by: the NCI, US (WCM SPORE in Prostate Cancer, P50CA211024-01, R37CA215040, and R01CA233650, C.E.B.), Damon Runyon Cancer Research Foundation, MetLife Foundation Family Clinical Investigator Award, US (to C.E.B.), and the Prostate Cancer Foundation, US (M.A.A. and D.L.).

Corresponding author

Christopher E. Barbieri

413 E 69th St, New York, NY 10021

Phone: +1 212 746 5562

Fax: 212-746-0975

chb9074@med.cornell.edu

43 **Conflict of interests**

44 C.E.B. is co-inventor on a patent issued to Weill Medical College of Cornell University on SPOP
45 mutations in prostate cancer. E.D. is an employee of GenomeDx, Inc. The authors declare no other
46 potential competing interests.

47

48

Abstract

The normal androgen receptor (AR) cistrome and transcriptional program are fundamentally altered in prostate cancer (PCa). Here, we show that *SPOP* mutations, an early event in prostate tumorigenesis, reshape the chromatin landscape and AR-directed transcriptional program in normal prostate cells. Induction of *SPOP* mutation results in DNA accessibility and AR binding patterns found in human PCa. Consistent with dependency on this AR reprogramming, castration of *SPOP* mutant mouse models results in the loss of neoplastic phenotypes. Finally, human *SPOP* mutant PCa show improved response to AR-targeted therapies. Together, these results show that a single genomic alteration may be sufficient to reprogram the chromatin of normal prostate cells toward oncogenic phenotypes and that *SPOP* mutant tumors may be preferentially dependent on AR signaling through this mechanism.

62 **Introduction**

63 The androgen receptor (AR) is a critical driver and key therapeutic target in prostate cancer
64 (PCa). In normal prostate epithelial cells, AR coordinates growth-suppressive effects and
65 differentiation programs (Heinlein and Chang, 2004; Taplin and Balk, 2004). During prostate
66 carcinogenesis, AR is reprogrammed to instead promote oncogenic transcriptional programs
67 (Pomerantz et al., 2015). However, the mechanisms of this reprogramming remain incompletely
68 understood.

69 Recurrent missense mutations in *SPOP* (Speckle Type BTB/POZ Protein) occur in about
70 10% of localized primary PCa cases (Cancer Genome Atlas Research, 2015; Li et al., 2020) and
71 are highly prostate-specific; they are rarely observed in other cancer types. *SPOP* mutations
72 nominate a distinct molecular subtype of human PCa (Barbieri et al., 2012; Cancer Genome Atlas
73 Research, 2015; Shoag et al., 2018), with defined genomic alterations, DNA methylation,
74 transcriptional signatures, and clinical characteristics (Barbieri et al., 2012; Boysen et al., 2015;
75 Cancer Genome Atlas Research, 2015; Liu et al., 2018). Furthermore, a variety of data suggest
76 that *SPOP* mutations occur early in the process of prostate tumorigenesis (Baca et al., 2013;
77 Boysen et al., 2015). SPOP acts as the substrate recognition component of a CUL3-E3 ubiquitin-
78 protein ligase complex (Zhuang et al., 2009), with prostate cancer-associated mutations affecting
79 substrate specificity. Substrates reported to be affected by *SPOP* mutations include AR itself (An
80 et al., 2014; Geng et al., 2014), the AR coactivators SRC3 (Geng et al., 2013), p300 (Blattner et
81 al., 2017), and TRIM24 (Blattner et al., 2017), and chromatin-associated proteins like DEK
82 (Theurillat et al., 2014) and DAXX (Bouchard et al., 2018). However, how mutations in *SPOP*
83 impact AR-directed transcriptional programs, and if this is required for tumor initiation and
84 progression, remains unclear.

85 Here we leverage the unique capabilities of 3D prostate organoids to define the epigenomic
86 and transcriptional landscape upon AR activation and utilize a genetically engineered mouse
87 (GEM) model conditionally expressing mutant *SPOP* (Blattner et al., 2017) to characterize the
88 impact of a single genomic alteration in genetically normal cells.

89

90 **Results**

91 *Chromatin changes in normal prostate organoids with androgen stimulation*

92 Compared to our understanding of AR function in PCa cell lines and tissues (Pomerantz et
93 al., 2015; Sharma et al., 2013; Stelloo et al., 2018), much less is known of the mechanisms
94 underlying AR-mediated transcriptional regulation in normal prostate cells. Thus, to define the
95 epigenomic response to AR activation, we generated 3D organoid models of murine prostate
96 epithelial cells (Karthaus et al., 2014). Upon establishment, these prostate organoids faithfully
97 mimicked prostate gland architecture (Karthaus et al., 2014) and immunohistochemical features
98 (Fig. S1a). To catalogue the function of AR in the normal prostate, we assessed genome-wide
99 changes in transcriptional profiles (RNA-seq), chromatin accessibility by assay for transposase-
100 accessible chromatin (ATAC-seq), and cistromes of H3K4me2, AR, and FOXA1 by chromatin
101 immunoprecipitation sequencing (ChIP-seq) post-treatment with 10 nM DHT (Fig. 1a).

102 Gene expression data (Fig. S1b) showed upregulation of known murine AR-regulated
103 genes (Carver et al., 2011) by androgens in intact organoids, but not those with CRISPR-mediated
104 deletion of Ar (sgAr). We successfully validated the transcriptional response by performing GSEA
105 on AR-regulated genes in prostate tissue (Carver et al., 2011) (Fig. 1b), confirming a relevant
106 transcriptional response in our organoid model system (Fig. S1 b-f).

107 To define AR-driven alterations in the chromatin landscape in normal prostate epithelial
108 cells, we performed ATAC-seq, as a proxy for genetic regulatory element activity (Fig. S1g-h and
109 Tables S1 and S2). We identified 26,681 high-confidence differentially accessible peaks between
110 DHT-treated and vehicle-treated prostate organoids (FDR < 0.01, Fig. S1i). Next, we performed
111 *de novo* motif analysis of the DHT-enriched versus depleted accessible elements, revealing
112 significant enrichment of the androgen response element (ARE) motif in DHT-treated cells, which
113 was associated with an increase in accessibility at these sites post DHT treatment (Fig. 1c). To
114 connect the DHT-responsive regulatory elements to AR-target genes in prostate tissue, we profiled
115 the ATAC-seq signal of androgen-regulated genes in the mouse prostate (Carver et al., 2011) (Fig.
116 1d). Subsequently, we performed functional enrichment analysis of the ATAC-seq defined DNA
117 regulatory elements and associated AR-induced genes in both prostate organoids and tissue, with
118 "transcription factor binding" and "chromatin (nucleosomal) binding" among the enriched
119 categories (Fig. 1e). Overall, our ATAC-seq analysis confirmed a robust and biologically relevant
120 response to androgens at the chromatin level.

121 Next, to nominate the accessible peaks directly regulated by AR binding, we profiled AR
122 localization genome-wide after DHT stimulation. Genome-wide localization of AR by ChIP-seq
123 resulted in 42,206 AR peaks (Table S1). Importantly, our motif analysis found that the canonical
124 ARE was the most enriched motif in this dataset, confirming the specificity of our signal. Further
125 analysis comparing motif enrichment against that of AR in human prostate tissue (Pomerantz et
126 al., 2015) uncovered a highly similar motif enrichment pattern ($r = 0.89$, $p < 0.001$) (Fig. 1f),
127 suggesting our models faithfully recapitulate critical features of AR signaling.

128 Integrative analysis across data types revealed distinct clusters of regulatory sites either
129 unique to baseline or AR stimulated conditions, or common between these, with associated

130 dominant transcription factors motifs (Fig. 1g, S1e-j). While nuclear hormone receptor motifs were
131 most enriched in dynamic peaks associated with DHT stimulation (cluster 2), regions with
132 chromatin accessibility enriched in basal conditions (cluster 1) or common (cluster 3) were
133 associated with AP-1 motifs (Fra-1 and Jun-B). AP-1 motifs are also common in AR ChIP-seq
134 from normal human prostate tissue (Figure 1f), consistent with an AR-directed role in non-
135 transformed prostate cells.

136 Together, these data demonstrate that androgen stimulation of prostate organoids results in
137 chromatin and transcriptional changes concordant between both murine and human prostate tissues
138 and provides needed insight into the molecular functions of AR in a genetically normal context in
139 addition to being a valuable resource to study early events which contribute to AR driven prostate
140 tumorigenesis. In addition, it is a valuable resource to study early events which contribute to AR
141 driven prostate tumorigenesis.

142

143 *SPOP mutation alone alters the landscape of accessible enhancers in response to androgen*

144 *SPOP* mutations are present in about 10% of PCa (Barbieri et al., 2012; Cancer Genome
145 Atlas Research, 2015; Li et al., 2020), occur early in the natural history of the disease, are relatively
146 prostate-specific, and affect AR activity through deregulation of multiple substrates (Blattner et
147 al., 2017; Geng et al., 2013; Theurillat et al., 2014). We previously developed a transgenic mouse
148 with Cre-dependent, conditional expression of SPOP-F133V (Fig. 2a) (Blattner et al., 2017). In
149 prostate organoids infected with the Cre virus and vector, we examined the impact of an *SPOP*
150 mutation on the epigenomic and transcriptional landscapes after androgen stimulation (Fig. 2b).

151 We profiled the chromatin accessibility landscape of androgen-stimulated prostate
152 organoids expressing mutant (Fig. S2a-c) and wildtype SPOP using ATAC-seq (Fig. S1g-i). We
153 found > 44.9k differentially accessible sites (Fig. 2c), the majority of which were not promoter-
154 associated, but at distal intergenic and intronic regions, consistent with enhancers (Fig. 2d).
155 Dynamic accessible peaks enriched in *SPOP* mutant organoids (Fig. 2e) were enriched for motifs
156 of TFs important for AR-driven prostate tumorigenesis (Fig. 2f), including FOXA1 and HOXB13
157 (Pomerantz et al., 2015). These data support that the chromatin landscape of *SPOP*-mutant prostate
158 cells is remodelled (Fig. S2d-e), especially at androgen-responsive enhancer regions associated
159 with lineage-specific, oncogenic transcription factors.

160 H3K4me2-marked nucleosomes go through remodelling upon AR binding to chromatin
161 (He et al., 2010). Upon androgen stimulation, the H3K4me2 nucleosome at the center of ARE is
162 evicted, and subsequently, AR-binding sites are flanked with H3K4me2 nucleosomes. The same
163 bimodal distribution before and after androgen stimulus was shown in the case of AR-pioneering
164 factor FOXA1 as well (He et al., 2010). Consistent with our chromatin accessibility data, there
165 was more pronounced chromatin remodelling (measured by H3K4me2) at AR bound enhancers in
166 *SPOP*-mutant organoids (Fig. 2g) that also showed a higher frequency of FOXA1 and joint
167 FOXA1:AR motifs.

168

169 *SPOP mutation drives an oncogenic AR-cistrome in prostate organoids*

170 Oncogenic reprogramming of the AR cistrome is a fundamental feature of prostate cancer
171 (Augello et al., 2019; Pomerantz et al., 2015; Sharma et al., 2013; Stelloo et al., 2018), but which
172 specific alterations can drive this phenotype, and what stage of the disease it occurs, remains
173 unclear. We sought to test the hypothesis that a single early event like *SPOP* mutation could impact

174 reprogramming of the AR cistrome to mimic PCa. AR ChIP-seq (Tables S1 and S2) with a
175 validated AR antibody, revealed 13,598 differential AR binding sites (FDR < 0.01) between
176 control and *SPOP*-mutant organoid lines (Fig. 3a). In *SPOP*-mutant organoids, the AR cistrome
177 was enriched for the motifs of well-established regulators of AR function associated with
178 tumorigenesis, including FOXA1 and HOXB13 (Fig. 3b). Strikingly, the motif enrichment pattern
179 in *SPOP*-mutant organoids compared to controls was remarkably similar to that of previously
180 reported in AR cistromes of human prostate adenocarcinoma (PRAD) samples (Pomerantz et al.,
181 2015) as compared to normal prostate tissue (Fig. S3a-b). Consistent with ATAC-seq results, AR
182 peaks in *SPOP*-mutant prostate organoids harbored a higher density of canonical AR and FOXA1
183 motifs (Fig. 3c-d). To validate the relevance of this shift in the TF motif occurrence, we analyzed
184 the AR cistromes of human primary prostate carcinoma tissue samples (Stelloo et al., 2018) (Fig.
185 3e). AR peaks from human *SPOP* mutant cancers had higher FOXA1 motif density (Fig. 3f),
186 associated with a shift in the binding of FOXA1 towards the center of AR peaks (Fig. 3g),
187 consistent with our murine organoid model. Collectively, these data suggest that that *SPOP*
188 mutation alone alters the androgen-responsive enhancer landscape, drives an AR cistrome
189 consistent with PCa, and nominates FOXA1 as a potential mediator of this phenotype.

190

191 *Increased FOXA1 binding in SPOP mutant tumors*

192 FOXA1 acts as a pioneer factor, binding and opening condensed chromatin via its winged-
193 helix DNA binding domains (Cirillo et al., 2002), facilitating AR-mediated transcriptional control
194 (Gao et al., 2003). To better define the role of FOXA1 nominated by motif enrichment in a subset
195 of SPOPmut-specific AR peaks (Fig. 3), we assessed genome-wide FOXA1 binding. *SPOP* mutant
196 organoids and controls showed 27,168 differential FOXA1 peaks (Fig. 4a, Table S1). Moreover,

197 the highest FOXA1, FOXA1:ARE, and ARE motif densities occurred within the SPOPmut-
198 specific FOXA1 cistrome (Fig. 4b). Next, we interrogated AR binding at FOXA1-bound enhancers
199 and found profound enhancement of AR signal at FOXA1-bound accessible enhancers specific for
200 *SPOP* mutant prostate cells (Fig. 4c-d). These data implicate a role for FOXA1 downstream of
201 *SPOP* mutation in driving pro-tumorigenic changes at a subset of AR binding loci.

202 We next looked in human prostate cancers for evidence to support a relationship between
203 *SPOP* mutation and FOXA1. *FOXA1* is recurrently mutated in localized prostate cancer, with
204 forkhead (FKHD) domain mutations altering pioneering activity being the most common (Adams
205 et al., 2019; Barbieri et al., 2012; Cancer Genome Atlas Research, 2015; Parolia et al., 2019). We
206 hypothesized that if *SPOP* mutations acted in part through modulation of FOXA1 activity, then
207 *SPOP*-mutant and *FOXA1*-mutant tumors would display similar features. When applying a
208 previously reported transcriptional classifier for *SPOP* mutation (Liu et al., 2018), the majority of
209 *FOXA*1 mutant tumors cluster together with *SPOP* mutant tumors (Figure 4e). In addition, tumors
210 harbouring *SPOP* mutations and those with *FOXA1* alteration display similar somatic copy number
211 alterations (Figure 4f), suggesting common collaborating events.

212

213 *Gene expression alterations in SPOP mutant prostate organoids*

214 To define whether the changes in accessibility and FOXA1 and AR binding are reflected
215 in transcriptional response to androgens in *SPOP* mutant cells, we performed RNA-seq (Fig. S4a-
216 b). Importantly, AR induced and repressed distinct genes in Control and SPOPmut cells (Fig. 5a).

217 We next sought to leverage multiple levels of data to define genes that are AR-regulated
218 specifically in the context of *SPOP* mutation (Fig. 5b). Integrative analysis of ATAC-seq, AR

219 ChIP-seq, and RNA-seq data nominated genes linked to dynamic regulatory events in *SPOP*
220 mutant mouse organoids, and dependent on AR for induction (n=2043). Of these, 753 genes were
221 also upregulated in *SPOP* mutant human prostate cancers (Fig. 5c), and these were used to generate
222 an *SPOP*-mutant AR signature score (Fig. 5d). By correlating across datatypes, we identified AR-
223 driven, SPOP mutation specific transcriptional regulatory events, with increased AR binding,
224 increased accessibility, and AR-dependent increased gene expression in genes such as *Abcc5* and
225 *Pdlim5*, which has been previously linked to prostate cancer pathogenesis (Liu et al., 2017).
226 Functional categorization of these *SPOP*-mutant specific AR-regulated genes revealed enrichment
227 for metabolic pathways, Nuclear receptor signaling, and cell cycle, consistent with an AR-
228 dependent role in prostate tumorigenesis (Fig. 5f). Together, we conclude that the SPOPmut
229 associated changes in accessibility and transcription factor binding drive a distinct AR-dependent
230 gene expression program, one more consistent with tumorigenesis.

231

232 *Critical dependency of SPOP mutant prostate epithelium on AR signaling*

233 Having observed that *SPOP* mutation alters the androgen-responsive chromatin landscape
234 and transcriptional program, we next examined whether *SPOP* mutant prostate organoids showed
235 increased dependency on AR signaling. *SPOP* mutant organoids showed increased sensitivity to
236 AR inhibition with bicalutamide compared to controls (Fig. 6a), with the proliferation of the
237 SPOPmut significantly more sensitive to anti-androgen treatment both in 2D and 3D growth
238 conditions (Fig. S5a-b). Given the importance of FOXA1 in the epigenomic alterations in *SPOP*-
239 mutant cells, we hypothesized that FOXA1 was necessary for the AR dependency driven by *SPOP*
240 mutation as well. Transient downregulation of FOXA1 further increased the sensitivity of
241 SPOPmut organoids to AR inhibition (Fig. 6b).

242 To investigate the role of AR signaling in a mouse model of *SPOP-F133V*, we performed
243 a pathologic analysis of castrate and hormonally intact mice in a background of heterozygous *Pten*
244 loss ($PbCre^{+};Pten^{L/+};Rosa26^{F133V}$). We have previously shown that *SPOP* mutation alone is
245 insufficient to drive tumorigenesis in mouse prostate (Blattner et al., 2017). However, in a
246 conditional *Pten* deleted background, *SPOP* mutation results in more aggressive neoplastic
247 histology, including high-grade PIN (HG-PIN) in $Pten^{L/+}$ mouse prostates and invasive carcinoma
248 in $Pten^{L/L}$. We castrated *SPOP* mutant ($PbCre^{+};Pten^{L/+};Rosa26^{F133V}$) and control ($PbCre^{+};Pten^{L/+}$)
249 mice at 8 weeks, sacrificed them at 9 months and performed a histological examination of their
250 prostates compared to age-matched uncastrated controls (Fig. 6c). Castration reversed the
251 increased amount of HG-PIN, nuclear atypia, and proliferation seen in *SPOP* mutant prostates
252 compared to controls (Fig. 6d-f and S5c-d). In the setting of homozygous *Pten* loss, *SPOP*-mutant
253 mice ($PbCre^{+};Pten^{L/L};Rosa26^{F133V}$) develop invasive, poorly differentiated carcinomas, while
254 control mice ($PbCre^{+};Pten^{L/L}$) developed only diffuse HG-PIN (Blattner et al., 2017). In this
255 background, we found that *SPOP* mutant castrated mice develop features of invasive disease less
256 frequently than hormonally intact mice, while the diffuse, proliferative HG-PIN in both *SPOP*
257 mutant mice and $Pten^{L/L}$ controls (Fig. 6g) remains relatively castration-resistant, consistent with
258 prior reports (Blattner et al., 2017; Mulholland et al., 2011). Together, these data show that
259 castration results in the reversal of *SPOP* mutant phenotypes *in vivo*, suggesting that these
260 phenotypes are driven by AR signaling.

261

262 *SPOP mutation is associated with improved response to AR-targeted therapies*

263 Given the prominent role of AR signaling in *SPOP* mutant preclinical models, we
264 investigated the impact of *SPOP* mutation on patient response to therapies targeting AR in multiple

265 clinical scenarios. Using a previously developed transcriptional classifier for the *SPOP* mutant
266 subclass (Liu et al., 2018), we examined data derived from the Decipher Genomics Resource
267 Information Database (GRID) registry (ClinicalTrials.gov identifier: NCT02609269) (Liu et al.,
268 2018). In a pooled retrospective cohort of 1,626 patients *SPOP* mutant tumors were associated
269 with improved metastasis (MET)-free survival in patients who received androgen deprivation
270 therapy (ADT) after radical prostatectomy, but no difference without ADT (Fig. 7a and Table S3).
271 Next, we hypothesized that preferential sensitivity to ADT would manifest with relative depletion
272 of *SPOP* mutant tumors in castrate-resistant prostate cancer compared to hormone-sensitive
273 disease. Comparing 333 primary prostate adenocarcinomas (Cancer Genome Atlas Research,
274 2015) and 414 metastatic CRPC samples (Abida et al., 2019), *SPOP* mutations were significantly
275 lower in CRPC (Fig. 7b), suggesting a response to ADT. To rule out an effect of primary vs.
276 metastatic disease in this analysis, we compared metastatic hormone-sensitive PCa (mHSPC) to
277 metastatic hormone-resistant PCa (mCRPC) within the same cohort (Abida et al., 2017), and again
278 observed significant underrepresentation of *SPOP* mutation in mCRPC, consistent with the
279 sensitivity of *SPOP* mutant metastatic prostate cancers to ADT (Fig. 7c). Finally, we examined
280 the response of patients with mCRPC patients to AR-targeted therapy (abiraterone and
281 enzalutamide) (Abida et al., 2019). *SPOP* mutation was associated with a longer time on treatment
282 in these patients, suggesting that AR-targeted therapies may be a more durable treatment option in
283 *SPOP* mutant prostate cancer than in other subtypes (Fig. 7d). Overall, all these results together
284 show a favourable outcome of *SPOP* mutant PCa to AR-targeted therapy across multiple clinical
285 scenarios and suggest that *SPOP* mutation may be a predictive biomarker for these therapeutic
286 regimens.

287

288 **Discussion**

289 The androgen receptor (AR) is the central determinant of prostate tissue identity and
290 differentiation (Cunha et al., 2004), controlling normal, growth-suppressive prostate-specific gene
291 expression (Schiewer et al., 2012). However, it is also a central driver of prostate tumorigenesis,
292 becoming "hijacked" to drive oncogenic transcription (Schiewer et al., 2012). Importantly, it also
293 remains the key therapeutic target for PCa, even in advanced castrate-resistant prostate cancer
294 (CRPC) (Watson et al., 2015). However, how AR function is altered to convert it to an oncogenic
295 factor, and at what steps in the process of tumorigenesis this occurs, remain poorly defined. Here,
296 we show that a single early event in the natural history of prostate cancer is sufficient to drive
297 oncogenic alterations in the AR-directed chromatin landscape and transcriptional program.

298 It has been long recognized that AR is required for the development and function of the
299 normal prostate (Heinlein and Chang, 2004). However, how AR reshapes the landscape of
300 chromatin to execute its transcriptional program, particularly in genetically normal cells, remains
301 unclear. Here, using genetically normal, physiologically relevant prostate organoids, we defined
302 the genome-wide effect of androgens on chromatin accessibility, H3K4me2, AR, and FOXA1
303 binding and subsequent changes in the transcriptome. These data provide insight to transcriptional
304 dynamics of normal AR function, and demonstrate that these genetically pliable models can
305 recapitulate the epigenomic and transcriptomic changes of mouse and human tissue, credentialing
306 a valuable tool to investigate AR activity.

307 Missense mutations in *SPOP* are the most common mutations in primary prostate
308 adenocarcinoma, occur early in the natural history of the disease and affect multiple substrate
309 proteins associated with AR-mediated transcriptional regulation (Blattner et al., 2017; Bouchard
310 et al., 2018; Geng et al., 2013; Geng et al., 2014; Theurillat et al., 2014). Here, we show that *SPOP*

311 mutation alone, in otherwise normal prostate organoids, is sufficient to induce dramatic changes
312 in accessibility of regulatory elements. Furthermore, *SPOP* mutation was sufficient to reprogram
313 the AR cistrome to one with striking resemblance to human PCa. Interestingly one other study
314 reported different effects on the AR cistrome in response to *SPOP* mutation introduced into
315 established cell lines with multiple alterations (Copeland et al., 2019), with expansion of the AR
316 cistrome towards both normal and tumorigenic sites. The more profound shift we report here may
317 reflect the utility of genetically normal models in studying initiation events, and suggest that
318 oncogenic reprogramming of the AR transcriptional program may be a very early event in the
319 natural history of PCa, at least in selected subtypes.

320 FOXA1 is a key pioneering factor for AR and HOXB13 transcription factors, facilitating
321 binding to at PCa-specific AR bound-sites. Furthermore, FOXA1 and HOXB13 overexpression
322 transforms AR cistrome from normal, immortalized cell lines into an oncogenic one (Copeland et
323 al., 2019; Pomerantz et al., 2015). Our study points to a significant role for FOXA1 during the
324 reprogramming of AR cistrome in *SPOP* mutant prostate organoids, consistent with observations
325 in human tumors.

326 The data here suggest that oncogenic reprogramming of AR-driven transcription is the
327 major mechanism underlying the oncogenic function of *SPOP* mutation in prostate cancer.
328 Consistent with this, we also find that functionally, *SPOP* mutant model systems show high
329 dependency on this pathway, and in clinical data, *SPOP* mutant human prostate cancers show
330 increased sensitivity to androgen-targeted therapy. Strikingly, our analysis of the data from
331 multiple clinical scenarios supports this hypothesis: patients receiving adjuvant or salvage ADT
332 after prostatectomy (Fig. 7a) and second generations AR inhibitors with CRPC (Fig. 7d), as well
333 depletion of *SPOP* mutation in CRPC compared to both primary and hormone sensitive metastatic

334 disease (Fig. 7b-c), consistent with reports of favourable outcomes for *SPOP* mutant cancers with
335 therapies targeting AR in both CRPC (Boysen et al., 2018) and hormone sensitive metastatic
336 disease (Swami et al., 2020). However, credentialing *SPOP* mutation as a clinically actionable
337 predictive biomarker for AR-directed therapies will require clinical trials designed for this purpose,
338 likely in each specific clinical scenario. Consistent with this, Tewari and colleagues report that
339 *SPOP* mutation is a truncal alteration in human prostate cancers that show exceptionally robust
340 response to neoadjuvant androgen-targeted therapy (in review). Together, these clinical data
341 suggest that the AR-dependent effects of *SPOP* mutation are not unique to a single clinical
342 scenario, but may extend to multiple stages of prostate cancer, broadening the potential impact.

343

344 **Methods**

345 *Transgenic mouse model*

346 Weill Cornell Medicine (WCM) Institutional Care and Use Committee approved all the
347 mouse studies under protocol 2015-0022. Transgenic mice had prostate-specific expression of
348 human *SPOP-F133V* in *Rosa26* locus (*PbCre;R26*$^{F133V/WT}$ or *PbCre;R26*$^{F133V/F133V}$) with or without
349 *Pten* deletion (*PbCre;R26*$^{F133V/WT}$;*Pten*$^{+/+}$, *PbCre;R26*$^{F133V/WT}$;*Pten*$^{L/+}$,
350 *PbCre;R26*$^{F133V/F133V}$;*Pten*$^{L/+}$ or *PbCre;R26*$^{F133V/WT}$;*Pten*$^{L/L}$)(Blattner et al., 2017). TransNetYX
351 performed mouse genotyping by using published primers (Augello et al., 2019; Blattner et al.,
352 2017).

353

354

355

356 *Immunohistochemistry*

357 Whole murine prostates were processed as previously described(Augello et al., 2019).
358 Staining was done at The Translational Research Program (TRP) of the Department of Pathology
359 and Laboratory Medicine at WCM. Ki67 (ab16667) was used for staining.

360

361 *Murine Organoid Line Generation and CRISPR experiments*

362 Prostate from the *PbCre4* negative; *Rosa26*^{F133V} mice were harvested at 1-2 months of age
363 and processed and grown as 3D Matrigel culture as previously described (Drost et al., 2016) with
364 the exception that the organoid media contained 5 ng/mL EGF. Lines were generated by infection
365 with Adeno-RFP (Control cells) or Adeno-Cre (SPOPmut cells) viruses (Augello et al., 2019). The
366 expression of the human *SPOP-F133V* transgene was confirmed by immunoblot. To knockout *Ar*
367 expression, the cells were infected with lentiviruses containing sgNT or sgAr gRNA in
368 pLentiCRISPRv2 plasmids (a kind gift from Dong Zhao, Sawyer's lab, MSK). Plasmid sequences
369 were verified by Sanger sequencing (Genewiz). Polyclonal populations resistant to puromycin
370 were subjected to immunoblot to verify AR protein expression.

371

372 *Immunofluorescence*

373 Organoids were resuspended Cell Recovery Solution (Corning) to melt the matrigel
374 without disrupting the 3D cellular organization. Organoids were pelleted and embedded into
375 fibrinogen and thrombin clots. These were transferred into embedding cassettes and fixed in 10%
376 formalin. The paraffin sections were prepared at The Translational Research Program of the
377 Department of Pathology and Laboratory Medicine at WCM. Immunofluorescent staining was

378 performed as described previously (Augello et al., 2019) by using anti-Ck5, anti-Ck8, and anti-
379 AR primary antibodies (Blattner et al., 2017).

380

381 *Pathology review*

382 All murine prostate sections were reviewed by board-certified genitourinary pathologists
383 with expertise in human and murine models of prostate cancer (B.D.R., F.K). All reviews were
384 performed blinded to genotype.

385

386 *Immunoblot*

387 Whole-cell protein lysates were prepared after digestion of Matrigel (Corning Cat#
388 356231) with TrypLE Express Enzyme (1X), phenol red (Gibco). Pelleted cells were washed in
389 PBS and lysed in RIPA buffer (Thermo Fisher Scientific, Cat# PI-89901) supplemented with
390 protease and phosphatase inhibitors (Thermo Fisher Scientific, Cat# 78441). Proteins were
391 quantified by BCA assay (Thermo Fisher Scientific, Cat# 23227) and separated on 4-15% Protein
392 Gels (BioRad, Cat# 4568084). SPOP protein was probed by using in-house made rabbit anti-SPOP
393 (1:1000); for AR and FOXA1, we used following rabbit antibodies: Abcam, ab108341 and Abcam,
394 ab23738. For loading control, we used anti-vinculin (ab129002).

395

396 *RNA-seq*

397 Murine organoids were grown for 6 days in media containing 1 nM DHT and then for 24
398 hr without DHT and EGF. Next, cells were stimulated with 10 nM DHT without EGF for 24 hr
399 and harvested for RNA-seq in biological quadruplicates. Total RNA was extracted, and DNaseI

400 treated by Maxwell 16 LEV simplyRNA Cells Kit (Promega, Cat# AS1270) and Maxwell nucleic-
401 acid extraction instrument (Promega). Nanodrop quantified RNA was checked by Bioanalyzer
402 RNA 6000 Nano Kit (Agilent Technologies). Samples with RNA integrity number > 10 were used
403 for library preparation (TruSeq Stranded mRNA Library Preparation (for Poly-A selection and
404 Stranded RNA-Seq) at the WCM Genomics Core. Libraries were sequenced twice on NextSeq500
405 (Illumina), High-output mode to generate 75 bp reads at WCM Genomics Core. Obtained FASTQ
406 files were aligned to the mm10 genome by using STAR v2.4.0j (Dobin et al., 2013). The reads
407 were counted with HTSeq (Anders et al., 2015). Differential gene expression was obtained in R
408 with DESeq2 v1.20.0 package (Anders and Huber, 2010). Gene set enrichment analysis
409 (Subramanian et al., 2005) was run in pre-ranked mode to identify enriched signatures in the
410 Molecular Signature Database (MSigDB).

411

412 *ATAC-seq*

413 Control and SPOPmut organoids were grown and treated as described for the RNA-seq
414 experiment. The experiment was performed in a biological quadruplicate. The single-cell
415 suspension was obtained after digesting organoids in TryPLE. ATAC-seq was performed on
416 100,00 nuclei as previously described (Grbesa et al., 2017) with the minor modifications. Nuclei
417 were isolated in buffer containing 10 mM Tris-Cl pH7.5, 10 mM NaCl, 3 mM $MgCl_2$, 0.1% Tween
418 (Sigma Millipore, Cat # 11332465001), 0.5% NP-40 (Sigma Millipore, Cat # 11332473001),
419 0.01% digitonin (Promega, Cat# G9441) and 1x protease inhibitors. Primers that were used for
420 quality checks of the libraries and for assessing mitochondrial DNA contamination are listed in
421 Table S2. Library size was checked with a Bioanalyzer 2100 system (Agilent Technologies) and
422 High Sensitivity DNA Kit (Agilent Technologies, Cat # 5067-4626). Generated DNA fragments

423 were quantified with Qubit dsDNA HS Assay Kit (Invitrogen, Cat # Q3285). Libraries were pooled
424 at equimolar concentration and submitted to WCM Genomics core, where they were paired-end
425 sequenced on HiSeq 4000 system (Illumina) with 50-bp reads. Raw FASTQ files were pre-
426 processed at WCM Genomics core.

427

428 *Bioinformatic processing of ATAC-seq data*

429 Quality control checks on raw sequence data were done with FASTQC v.0.11.8
430 (http://www.bioinformatics.babraham.ac.uk/projects/fastqc/). Paired-end reads were aligned to the
431 mm10 genome using Bowtie2 v.2.3.4.1 in a very sensitive mode. BAM files were sorted and
432 indexed with SAMtools v.1.8. The percentage of mitochondrial reads (Table S1) was calculated
433 with SAMtools using a custom script. All non-unique reads and mitochondrial reads were removed
434 before peak calling. Bigwig files were generated with deepTools v.3.3.1 (Ramirez et al., 2016)
435 bamCoverage tools from reads with min. mapping quality of 10 and using RPGC normalization.
436 Generated bigwig files were visualized with UCSC Genome Browser. Coverage at TSS of RefSeq
437 genes was done with deepTools computeMatrix and plotHeatmap tools (Fig. S1c). The fraction of
438 reads in peaks (FRiP) score was calculated by custom script by using BEDtools2 v.2.27 (Quinlan
439 and Hall, 2010) and reported in Table S1. Data quality was confirmed using Encode guidelines.
440 Peaks were called using Genrich (https://github.com/jsh58/Genrich), as explained on the Harvard
441 Bioinformatics site (https://informatics.fas.harvard.edu/atac-seq-guidelines.html). As an
442 additional quality control metric, we plotted insert size distribution which confirmed nucleosome-
443 free, mono-and di-nucleosomal distribution of the reads (Fig S1d, S2b). Consensus peaks for each
444 cell type and condition from 4 biological replicas were generated with DiffBind v.3.10 package
445 (Ross-Innes et al., 2012). Differential peak identification (in EdgeR (McCarthy et al., 2012), FDR

446 < 0.01), MA plots, and volcano plots were done in the R software environment v.3.6.0 (The R
447 Foundation) by using DiffBind.

448 Assignment of ATAC-seq peaks to genes – One Mb regions around the transcription start
449 sites of selected genes were retrieved through the UCSC Table Browser program. Then they were
450 intersected with the bed file containing ATAC-seq peak regions.

451 Annotation of Genomic Regions – *Cis*-regulatory element analysis of consensus and
452 differential ATAC-seq peaks was performed with the annotatePeaks.pl of Homer v.4.10 software
453 (Heinz et al., 2010). The stacked barplot of enrichment of genomic regions was created in R v3.6.0
454 with a ggplot2 v3.2.1 package.

455 Integration with RNA-seq data –was done via Cistrome-GO webserver (Li et al., 2019).

456

457 *ChIP-seq experiments and bioinformatic data processing*

458 Control and SPOPmut organoids were grown and treated in biological triplicates, as
459 described in the RNA-seq section. For H3K4me2 ChIP single-cell suspension was crosslinked
460 with 1% methanol-free formaldehyde (Thermo Scientific Pierce, Cat #PI-28906) at 37°C. For AR
461 and FOXA1 ChIP organoids were double fixed (Singh et al., 2019) with 2 mM Di(N-succinimidyl)
462 glutarate (Millipore Signal, Cat #80424-5MG-F) and then 1% formaldehyde. Crosslinking was
463 quenched with 125 mM glycine. The crosslinked organoid pellets were snap-frozen and stored at
464 -80 °C until use. Samples were thawed on ice, lysed in 1% SDS containing buffer supplemented
465 with 1x protease and phosphatase inhibitors, and sonicated for 4 x 10 cycles (30 sec on, 30 sec off)
466 in temperature-controlled Bioruptor 300 (Diagenode). Debris was removed by centrifuging at
467 14,000 rpm at 4°C. One percent of the supernatant was saved as input, and the rest was added to

468 antibody-coupled Dynabead Protein A (Thermo Fisher Scientific, Cat #10001D) and incubated
469 overnight rocking at 4 °C. Used antibodies were: anti-H3K4me2 ChIP-grade (ab7766), anti-AR
470 PG-21 (Millipore, Cat # 06-680) and anti-FOXA1 ChIP-grade (ab23738). Chromatin was washed
471 on ice with 2x each standard wash buffers (Low-Salt, High-Salt, and LiCl) and finally with TE.
472 Decrosslinking of input and immunoprecipitated chromatin was performed in buffer containing
473 1% SDS, 0.3M NaCl, and 0.2 mg/mL Proteinase K (Thermo Fisher Scientific, Cat #AM2548) for
474 16 hr at 65 °C. After 2 hr incubation with RNase A (Thermo Fisher Scientific, Cat #EN0531)
475 decrosslinked material was purified with 2 x AMPure XP beads (Beckman Coulter, Cat #A63881)
476 and eluted in 30 μL of 10 mM Tris-Cl, pH 8. The DNA concentration was measured by Qubit
477 dsDNA HS Assay Kit (Thermo Fisher Scientific, Cat # Q32851). Individual ChIP samples were
478 verified by qPCR (primers are listed in Table S2). Libraries were prepared by NEBNext Ultra II
479 DNA Library Prep (New England Biolabs, Cat #E7645S) by using NEBNext Multiplex Oligos for
480 Illumina (New England Biolabs, Cat #E7335S and #E7500S). Library size and presence of
481 adapters was verified by Bioanalyzer HS DNA chips (Agilent Technologies, Cat# 5067-4626).
482 Libraries passing the quality control were pooled and sequenced at WCM Genomics core for 50
483 cycles on HiSeq4000 to generate single-end 50-bp reads. Generated FASTQ files were validated
484 for quality using FastQC v.0.11.8 software and processed with ENCODE ChIP-seq pipeline
485 (https://github.com/ENCODE-DCC/chip-seq-pipeline2). All reads were aligned to mouse genome
486 mm10. Briefly, this pipeline generated an HTML-quality report from which we inferred the overall
487 quality of our ChIP-seq. Only the samples passing the ENCODE-specified NSC, RCS, FRiP, and
488 PBC metrics (Landt et al., 2012) (https://www.encodeproject.org/data-standards/chip-seq/) were
489 included in further data analysis (Table S1). All the peaks were called with MACS2(Zhang et al.,

490 2008) at the p-value threshold of 0.05. Differential peak analysis was performed by DiffBind in
491 EdgeR mode with 0.01 FDR cutoff.

492

493 *Motif Enrichment Analysis*

494 *De novo* and known motif analysis of ATAC-seq and ChIP-seq consensus or differential
495 peaks was done by findMotifsGenome.pl program within Homer v.4.10 software. For the analysis
496 of H3K4me2 peaks, we used -size given option, while for the rest of the data, we analyzed 200 bp
497 region around the peak summit. To determine motif enrichment between two datasets with similar
498 peak numbers, one served as a background (-bg flag) for the other. For the enhancer-specific motif
499 scanning, peaks localized to promoter and 5'UTR were removed before the analysis. To create
500 motif density histograms the analyzed peaks were centered on the specific motif, and the analysis
501 was run by findMotifsGenome.pl in a histogram mode (-hist with 5 bp bin size) and visualized
502 with GraphPad Prism v8.2.1. Motif analysis of human primary prostate tumors (Stelloo et al.,
503 2018) was done as previously described (Augello et al., 2019) with the only difference that the AR
504 peaks were binned according to the presence or absence of *SPOP* mutation. All the other plots
505 were generated in R with ggplot2 v3.2.1 package.

506

507 *Copy number analysis*

508 The copy number alterations of PRAD were downloaded from TCGA portal
509 (https://portal.gdc.cancer.gov/) via gdc-client tool. Fraction of altered cases within *SPOP* and
510 *FOXA1* mutant subclasses were calculated respectively. Segments with log2-ratio >0.3 were
511 defined as genomic amplifications, and log2-ratio < –0.3 were defined as genomic deletions.

512

513 *3D organoid growth assay*

514 Five thousand cells were seeded in 10 μL of matrigel plug (Corning Matrigel Basement
515 Membrane Matrix, Growth Factor Reduced) per well (Corning 96 well assay, flat bottom clear,
516 black, polystyrene plate) in 100 μL of mouse organoid media (Blattner et al., 2017) without EGF
517 and with 0.01 nM DHT. Cells were allowed to form organoids for four days before the
518 bicalutamide treatment. Drug treated cells were assayed for cell viability after four days with
519 CellTiter-Glo 3D assay (Promega), as per manufacturer's instructions. The experiment was
520 repeated for a total of four biological repeats (technical triplicate for each treatment).
521 Luminescence readings (BioTek Synergy Neo microplate reader with Gen5 software) were
522 analyzed with GraphPad Prism 8.2.1 according to the instructions for the analysis of dose-response
523 data.

524

525 *siRNA mediated FOXA1 knockdown*

526 Transient knockdown of *Foxa1* was done by transfecting mouse organoid cells grown on
527 the surface of collagen I coated plates with siRNA (SMARTpool: siGENOME Foxa1 siRNA). For
528 the control, we used the same concentration of scrambled siRNA (siGENOME Non-Targeting
529 Control siRNA Pool). Transfection was done with Lipofectamine RNAiMAX according to the
530 manufacturer's instructions. After four hours media was replaced and cells were lifted and plated
531 into Matrigel plugs. Bicalutamide treatment and cell viability assay were performed as described
532 above.

533

534 *Clinical data analysis*

535 We have developed a novel gene expression signature, classifier SCaPT (Subclass
536 Predictor Based on Transcriptional Data), and decision tree to predict the *SPOP* mutant subclass
537 from RNA gene expression data (Liu et al., 2018). We then classified the *SPOP* mutant subclass
538 in a Decipher retrospective cohort of 1,626 patients (Table S3) (Liu et al., 2018) and evaluated the
539 associations between *SPOP* mutant status and patient outcomes of metastasis mortality with and
540 without ADT treatment based on Kaplan-Meier (KM) analysis.

541 Prevalence of *SPOP* mutation was analyzed on cBioPortal v3.2.0 platform (Cerami et al.,
542 2012) by using the following datasets (accessed on January 2020): Prostate Adenocarcinoma
543 (TCGA, Cell 2015) (Cancer Genome Atlas Research, 2015), Metastatic Prostate Adenocarcinoma
544 (SU2C/PCF Dream Team) (Abida et al., 2019) and Prostate Cancer (MSKCC) (Abida et al., 2017).
545 For time on ADT analysis, patient's data from cBioPortal and GitHub
546 (https://github.com/cBioPortal/datahub/tree/master/public/prad_su2c_2019) were combined in R
547 v3.6.0. KM analysis and plots were done in R using packages survival 2.44-1.1 and survminer
548 v0.4.6.

549

550 **Acknowledgments**

551 We are indebted to prostate cancer patients and families who contributed to this research. We thank
552 Dr. Dawid Nowak (WCM) and Dr. Jonathan E. Shoag (WCM) for helpful discussion. We thank
553 Dr. Daphne Campigli Di Giammartino (WCM) for helpful advice regarding ChIP-seq experiments.
554 We thank Dr. Mark Rubin for his mentorship and guidance in developing these projects and
555 reagents. We thank Weill Cornell Medicine (WCM) Genomics Core Facility, the Biospecimen and

556 Pathology Core of WCM SPORE in Prostate Cancer and Memorial Sloan Kettering Cancer Center
557 cBioPortal. We are grateful to Dr. Eric Klein, Dr. Bruce J. Trock, Dr. R. Jeffrey Karnes and Dr.
558 Robert B. Den for patient data.
559

560 **References**

561 Abida, W., Armenia, J., Gopalan, A., Brennan, R., Walsh, M., Barron, D., Danila, D., Rathkopf,
562 D., Morris, M., Slovin, S.*, et al.* (2017). Prospective Genomic Profiling of Prostate Cancer
563 Across Disease States Reveals Germline and Somatic Alterations That May Affect Clinical
564 Decision Making. JCO Precis Oncol *2017*.

565 Abida, W., Cyrta, J., Heller, G., Prandi, D., Armenia, J., Coleman, I., Cieslik, M., Benelli, M.,
566 Robinson, D., Van Allen, E.M.*, et al.* (2019). Genomic correlates of clinical outcome in
567 advanced prostate cancer. Proc Natl Acad Sci U S A *116*, 11428-11436.

568 Adams, E.J., Karthaus, W.R., Hoover, E., Liu, D.L., Gruet, A., Zhang, Z.D., Cho, H., DiLoreto,
569 R., Chhangawala, S., Liu, Y.*, et al.* (2019). FOXA1 mutations alter pioneering activity,
570 differentiation and prostate cancer phenotypes. Nature *571*, 408-+.

571 An, J., Wang, C., Deng, Y., Yu, L., and Huang, H. (2014). Destruction of full-length androgen
572 receptor by wild-type SPOP, but not prostate-cancer-associated mutants. Cell Rep *6*, 657-669.

573 Anders, S., and Huber, W. (2010). Differential expression analysis for sequence count data.
574 Genome Biol *11*, R106.

575 Anders, S., Pyl, P.T., and Huber, W. (2015). HTSeq--a Python framework to work with high-
576 throughput sequencing data. Bioinformatics *31*, 166-169.

577 Augello, M.A., Liu, D., Deonarine, L.D., Robinson, B.D., Huang, D., Stelloo, S., Blattner, M.,
578 Doane, A.S., Wong, E.W.P., Chen, Y.*, et al.* (2019). CHD1 Loss Alters AR Binding at Lineage-
579 Specific Enhancers and Modulates Distinct Transcriptional Programs to Drive Prostate
580 Tumorigenesis. Cancer Cell *35*, 817-819.

581 Baca, S.C., Prandi, D., Lawrence, M.S., Mosquera, J.M., Romanel, A., Drier, Y., Park, K.,
582 Kitabayashi, N., MacDonald, T.Y., Ghandi, M.*, et al.* (2013). Punctuated evolution of prostate
583 cancer genomes. Cell *153*, 666-677.
584 Barbieri, C.E., Baca, S.C., Lawrence, M.S., Demichelis, F., Blattner, M., Theurillat, J.P., White,
585 T.A., Stojanov, P., Van Allen, E., Stransky, N.*, et al.* (2012). Exome sequencing identifies
586 recurrent SPOP, FOXA1 and MED12 mutations in prostate cancer. Nat Genet *44*, 685-689.
587 Blattner, M., Liu, D., Robinson, B.D., Huang, D., Poliakov, A., Gao, D., Nataraj, S., Deonarine,
588 L.D., Augello, M.A., Sailer, V.*, et al.* (2017). SPOP Mutation Drives Prostate Tumorigenesis In
589 Vivo through Coordinate Regulation of PI3K/mTOR and AR Signaling. Cancer Cell *31*, 436-
590 451.
591 Bouchard, J.J., Otero, J.H., Scott, D.C., Szulc, E., Martin, E.W., Sabri, N., Granata, D., Marzahn,
592 M.R., Lindorff-Larsen, K., Salvatella, X.*, et al.* (2018). Cancer Mutations of the Tumor
593 Suppressor SPOP Disrupt the Formation of Active, Phase-Separated Compartments. Mol Cell
594 *72*, 19-36 e18.
595 Boysen, G., Barbieri, C.E., Prandi, D., Blattner, M., Chae, S.S., Dahija, A., Nataraj, S., Huang,
596 D., Marotz, C., Xu, L.*, et al.* (2015). SPOP mutation leads to genomic instability in prostate
597 cancer. Elife *4*.
598 Boysen, G., Rodrigues, D.N., Rescigno, P., Seed, G., Dolling, D., Riisnaes, R., Crespo, M.,
599 Zafeiriou, Z., Sumanasuriya, S., Bianchini, D.*, et al.* (2018). SPOP-Mutated/CHD1-Deleted
600 Lethal Prostate Cancer and Abiraterone Sensitivity. Clin Cancer Res *24*, 5585-5593.
601 Cancer Genome Atlas Research, N. (2015). The Molecular Taxonomy of Primary Prostate
602 Cancer. Cell *163*, 1011-1025.

603 Carver, B.S., Chapinski, C., Wongvipat, J., Hieronymus, H., Chen, Y., Chandarlapaty, S., Arora,
604 V.K., Le, C., Koutcher, J., Scher, H.*, et al.* (2011). Reciprocal feedback regulation of PI3K and
605 androgen receptor signaling in PTEN-deficient prostate cancer. Cancer Cell *19*, 575-586.
606 Cerami, E., Gao, J., Dogrusoz, U., Gross, B.E., Sumer, S.O., Aksoy, B.A., Jacobsen, A., Byrne,
607 C.J., Heuer, M.L., Larsson, E.*, et al.* (2012). The cBio cancer genomics portal: an open platform
608 for exploring multidimensional cancer genomics data. Cancer Discov *2*, 401-404.
609 Cirillo, L.A., Lin, F.R., Cuesta, I., Friedman, D., Jarnik, M., and Zaret, K.S. (2002). Opening of
610 compacted chromatin by early developmental transcription factors HNF3 (FoxA) and GATA-4.
611 Mol Cell *9*, 279-289.
612 Copeland, B.T., Du, J., Pal, S.K., and Jones, J.O. (2019). Factors that influence the androgen
613 receptor cistrome in benign and malignant prostate cells. Mol Oncol *13*, 2616-2632.
614 Cunha, G.R., Ricke, W., Thomson, A., Marker, P.C., Risbridger, G., Hayward, S.W., Wang,
615 Y.Z., Donjacour, A.A., and Kurita, T. (2004). Hormonal, cellular, and molecular regulation of
616 normal and neoplastic prostatic development. J Steroid Biochem Mol Biol *92*, 221-236.
617 Dobin, A., Davis, C.A., Schlesinger, F., Drenkow, J., Zaleski, C., Jha, S., Batut, P., Chaisson,
618 M., and Gingeras, T.R. (2013). STAR: ultrafast universal RNA-seq aligner. Bioinformatics *29*,
619 15-21.
620 Drost, J., Karthaus, W.R., Gao, D., Driehuis, E., Sawyers, C.L., Chen, Y., and Clevers, H.
621 (2016). Organoid culture systems for prostate epithelial and cancer tissue. Nat Protoc *11*, 347-
622 358.
623 Gao, N., Zhang, J., Rao, M.A., Case, T.C., Mirosevich, J., Wang, Y., Jin, R., Gupta, A., Rennie,
624 P.S., and Matusik, R.J. (2003). The role of hepatocyte nuclear factor-3 alpha (Forkhead Box A1)

625 and androgen receptor in transcriptional regulation of prostatic genes. Mol Endocrinol *17*, 1484-
626 1507.
627 Geng, C., He, B., Xu, L., Barbieri, C.E., Eedunuri, V.K., Chew, S.A., Zimmermann, M., Bond,
628 R., Shou, J., Li, C.*, et al.* (2013). Prostate cancer-associated mutations in speckle-type POZ
629 protein (SPOP) regulate steroid receptor coactivator 3 protein turnover. Proc Natl Acad Sci U S
630 A *110*, 6997-7002.
631 Geng, C., Rajapakshe, K., Shah, S.S., Shou, J., Eedunuri, V.K., Foley, C., Fiskus, W., Rajendran,
632 M., Chew, S.A., Zimmermann, M.*, et al.* (2014). Androgen receptor is the key transcriptional
633 mediator of the tumor suppressor SPOP in prostate cancer. Cancer Res *74*, 5631-5643.
634 Grbesa, I., Tannenbaum, M., Sarusi-Portuguez, A., Schwartz, M., and Hakim, O. (2017).
635 Mapping Genome-wide Accessible Chromatin in Primary Human T Lymphocytes by ATAC-
636 Seq. J Vis Exp.
637 He, H.H., Meyer, C.A., Shin, H., Bailey, S.T., Wei, G., Wang, Q., Zhang, Y., Xu, K., Ni, M.,
638 Lupien, M.*, et al.* (2010). Nucleosome dynamics define transcriptional enhancers. Nat Genet *42*,
639 343-347.
640 Heinlein, C.A., and Chang, C. (2004). Androgen receptor in prostate cancer. Endocr Rev *25*,
641 276-308.
642 Heinz, S., Benner, C., Spann, N., Bertolino, E., Lin, Y.C., Laslo, P., Cheng, J.X., Murre, C.,
643 Singh, H., and Glass, C.K. (2010). Simple combinations of lineage-determining transcription
644 factors prime cis-regulatory elements required for macrophage and B cell identities. Mol Cell *38*,
645 576-589.

646 Hieronymus, H., Lamb, J., Ross, K.N., Peng, X.P., Clement, C., Rodina, A., Nieto, M., Du, J.,
647 Stegmaier, K., Raj, S.M., *et al.* (2006). Gene expression signature-based chemical genomic
648 prediction identifies a novel class of HSP90 pathway modulators. Cancer Cell *10*, 321-330.
649 Karthaus, W.R., Iaquinta, P.J., Drost, J., Gracanin, A., van Boxtel, R., Wongvipat, J., Dowling,
650 C.M., Gao, D., Begthel, H., Sachs, N., *et al.* (2014). Identification of multipotent luminal
651 progenitor cells in human prostate organoid cultures. Cell *159*, 163-175.
652 Landt, S.G., Marinov, G.K., Kundaje, A., Kheradpour, P., Pauli, F., Batzoglou, S., Bernstein,
653 B.E., Bickel, P., Brown, J.B., Cayting, P., *et al.* (2012). ChIP-seq guidelines and practices of the
654 ENCODE and modENCODE consortia. Genome Res *22*, 1813-1831.
655 Li, J., Xu, C., Lee, H.J., Ren, S., Zi, X., Zhang, Z., Wang, H., Yu, Y., Yang, C., Gao, X., *et al.*
656 (2020). A genomic and epigenomic atlas of prostate cancer in Asian populations. Nature *580*, 93-
657 99.
658 Li, S., Wan, C., Zheng, R., Fan, J., Dong, X., Meyer, C.A., and Liu, X.S. (2019). Cistrome-GO: a
659 web server for functional enrichment analysis of transcription factor ChIP-seq peaks. Nucleic
660 Acids Res *47*, W206-W211.
661 Liu, D., Takhar, M., Alshalalfa, M., Erho, N., Shoag, J., Jenkins, R.B., Karnes, R.J., Ross, A.E.,
662 Schaeffer, E.M., Rubin, M.A., *et al.* (2018). Impact of the SPOP Mutant Subtype on the
663 Interpretation of Clinical Parameters in Prostate Cancer. JCO Precis Oncol *2018*.
664 Liu, X., Chen, L., Huang, H., Lv, J.M., Chen, M., Qu, F.J., Pan, X.W., Li, L., Yin, L., Cui, X.G.,
665 *et al.* (2017). High expression of PDLIM5 facilitates cell tumorigenesis and migration by
666 maintaining AMPK activation in prostate cancer. Oncotarget *8*, 98117-98134.

667 McCarthy, D.J., Chen, Y., and Smyth, G.K. (2012). Differential expression analysis of
668 multifactor RNA-Seq experiments with respect to biological variation. Nucleic Acids Res *40*,
669 4288-4297.
670 Mulholland, D.J., Tran, L.M., Li, Y., Cai, H., Morim, A., Wang, S., Plaisier, S., Garraway, I.P.,
671 Huang, J., Graeber, T.G.*, et al.* (2011). Cell autonomous role of PTEN in regulating castration-
672 resistant prostate cancer growth. Cancer Cell *19*, 792-804.
673 Parolia, A., Cieslik, M., Chu, S.C., Xiao, L.B., Ouchi, T., Zhang, Y.P., Wang, X.J., Vats, P.,
674 Cao, X.H., Pitchiaya, S.*, et al.* (2019). Distinct structural classes of activating FOXA1 alterations
675 in advanced prostate cancer. Nature *571*, 413-+.
676 Pomerantz, M.M., Li, F., Takeda, D.Y., Lenci, R., Chonkar, A., Chabot, M., Cejas, P., Vazquez,
677 F., Cook, J., Shivdasani, R.A.*, et al.* (2015). The androgen receptor cistrome is extensively
678 reprogrammed in human prostate tumorigenesis. Nat Genet *47*, 1346-1351.
679 Quinlan, A.R., and Hall, I.M. (2010). BEDTools: a flexible suite of utilities for comparing
680 genomic features. Bioinformatics *26*, 841-842.
681 Ramirez, F., Ryan, D.P., Gruning, B., Bhardwaj, V., Kilpert, F., Richter, A.S., Heyne, S.,
682 Dundar, F., and Manke, T. (2016). deepTools2: a next generation web server for deep-
683 sequencing data analysis. Nucleic Acids Res *44*, W160-165.
684 Ross-Innes, C.S., Stark, R., Teschendorff, A.E., Holmes, K.A., Ali, H.R., Dunning, M.J., Brown,
685 G.D., Gojis, O., Ellis, I.O., Green, A.R.*, et al.* (2012). Differential oestrogen receptor binding is
686 associated with clinical outcome in breast cancer. Nature *481*, 389-393.
687 Schiewer, M.J., Augello, M.A., and Knudsen, K.E. (2012). The AR dependent cell cycle:
688 mechanisms and cancer relevance. Mol Cell Endocrinol *352*, 34-45.

689 Sharma, N.L., Massie, C.E., Ramos-Montoya, A., Zecchini, V., Scott, H.E., Lamb, A.D.,
690 MacArthur, S., Stark, R., Warren, A.Y., Mills, I.G.*, et al.* (2013). The androgen receptor induces
691 a distinct transcriptional program in castration-resistant prostate cancer in man. Cancer Cell *23*,
692 35-47.
693 Shoag, J., Liu, D., Blattner, M., Sboner, A., Park, K., Deonarine, L., Robinson, B.D., Mosquera,
694 J.M., Chen, Y., Rubin, M.A.*, et al.* (2018). SPOP mutation drives prostate neoplasia without
695 stabilizing oncogenic transcription factor ERG. J Clin Invest *128*, 381-386.
696 Singh, A.A., Schuurman, K., Nevedomskaya, E., Stelloo, S., Linder, S., Droog, M., Kim, Y.,
697 Sanders, J., van der Poel, H., Bergman, A.M.*, et al.* (2019). Optimized ChIP-seq method
698 facilitates transcription factor profiling in human tumors. Life Sci Alliance *2*, e201800115.
699 Stelloo, S., Nevedomskaya, E., Kim, Y., Schuurman, K., Valle-Encinas, E., Lobo, J., Krijgsman,
700 O., Peeper, D.S., Chang, S.L., Feng, F.Y.*, et al.* (2018). Integrative epigenetic taxonomy of
701 primary prostate cancer. Nat Commun *9*, 4900.
702 Subramanian, A., Tamayo, P., Mootha, V.K., Mukherjee, S., Ebert, B.L., Gillette, M.A.,
703 Paulovich, A., Pomeroy, S.L., Golub, T.R., Lander, E.S.*, et al.* (2005). Gene set enrichment
704 analysis: a knowledge-based approach for interpreting genome-wide expression profiles. Proc
705 Natl Acad Sci U S A *102*, 15545-15550.
706 Swami, U., Isaacsson Velho, P., Nussenzveig, R., Chipman, J., Sacristan Santos, V., Erickson,
707 S., Dharmaraj, D., Alva, A.S., Vaishampayan, U.N., Esther, J.*, et al.* (2020). Association of
708 SPOP Mutations with Outcomes in Men with De Novo Metastatic Castration-sensitive Prostate
709 Cancer. Eur Urol.
710 Taplin, M.E., and Balk, S.P. (2004). Androgen receptor: a key molecule in the progression of
711 prostate cancer to hormone independence. J Cell Biochem *91*, 483-490.

712 Theurillat, J.P., Udeshi, N.D., Errington, W.J., Svinkina, T., Baca, S.C., Pop, M., Wild, P.J.,
713 Blattner, M., Groner, A.C., Rubin, M.A., *et al.* (2014). Prostate cancer. Ubiquitylome analysis
714 identifies dysregulation of effector substrates in SPOP-mutant prostate cancer. Science *346*, 85-
715 89.
716 Watson, P.A., Arora, V.K., and Sawyers, C.L. (2015). Emerging mechanisms of resistance to
717 androgen receptor inhibitors in prostate cancer. Nat Rev Cancer *15*, 701-711.
718 Zhang, Y., Liu, T., Meyer, C.A., Eeckhoute, J., Johnson, D.S., Bernstein, B.E., Nusbaum, C.,
719 Myers, R.M., Brown, M., Li, W., *et al.* (2008). Model-based analysis of ChIP-Seq (MACS).
720 Genome Biol *9*, R137.
721 Zhuang, M., Calabrese, M.F., Liu, J., Waddell, M.B., Nourse, A., Hammel, M., Miller, D.J.,
722 Walden, H., Duda, D.M., Seyedin, S.N., *et al.* (2009). Structures of SPOP-substrate complexes:
723 insights into molecular architectures of BTB-Cul3 ubiquitin ligases. Mol Cell *36*, 39-50.

724

725

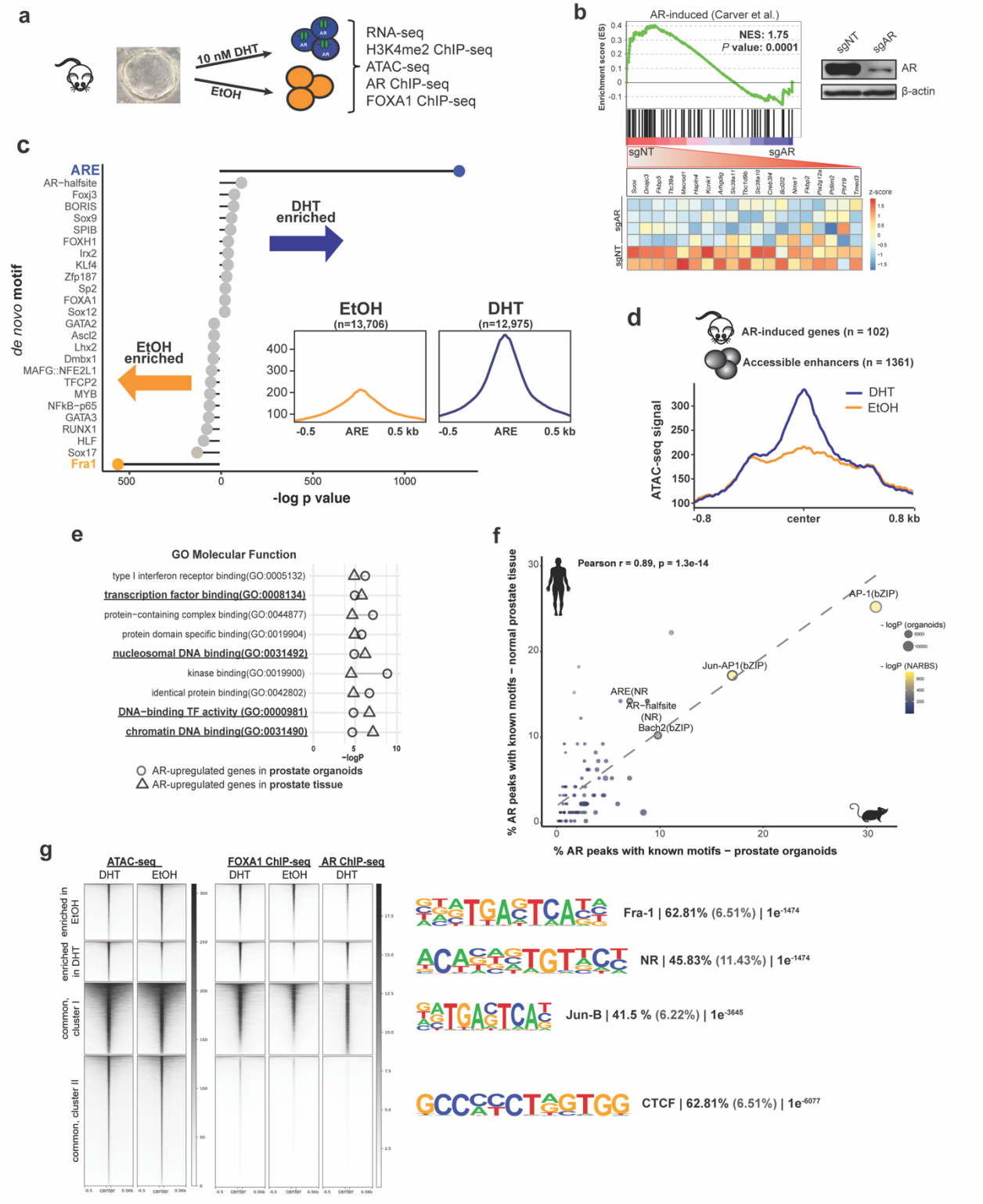

Fig. 1. DHT-induced changes in chromatin accessibility correspond to AR-transcriptional response. (a) Schematic representation of treatments and obtained datasets. **(b)** GSEA and leading

729 edge analysis of AR activity in normal prostate organoids. Upper right corner: Immunoblot of
730 murine organoid CRISPR-Cas9 cells with non-targeting (NT) or *Ar*-specific sgRNA. **(c)** Lolipop
731 plot representing known motif enrichment in vehicle-treated and androgen-treated murine
732 organoids. **(d)** Histogram depicting accessibility signal from EtOH-treated and DHT-treated
733 organoids over the center of regulatory elements within 1 Mb of AR-induced genes from prostate
734 tissue. **(e)** Cleveland plot indicating results of gene ontology (GO) analysis of AR-induced genes
735 in prostate organoids (circle) and prostate tissue (triangles) integrated with accessible regions
736 identified after androgen stimulation of organoid cells. **(f)** Known motif analysis of AR ChIP-seq
737 datasets from normal mouse organoids (x-axis) and human normal prostate tissue (n = 7; GEO:
738 GSE70079; y-axis) demonstrating enrichment for similar motifs ($r = 0.89$, $p < 0.001$). The dotted
739 line represents a regression line. Circle size represents the -log P-value of motif enrichment in AR
740 ChIP-seq peaks in normal murine prostate organoids and circle color the motif enrichment
741 significance in AR binding sites in normal prostate tissue (NARBS). **(g)** ATAC-seq, FOXA1, and
742 AR ChiP-seq signals over the regions that were identified to be more open before (enriched in
743 EtOH) or after androgens (enriched in DHT). The tornado plots also cover the regions whose
744 accessibility is not DHT-dependent (common). The most enriched *de novo* motifs per cluster are
745 depicted on the right, along with the percentage of target (black) and background (grey) regions
746 and the resulting p-value.

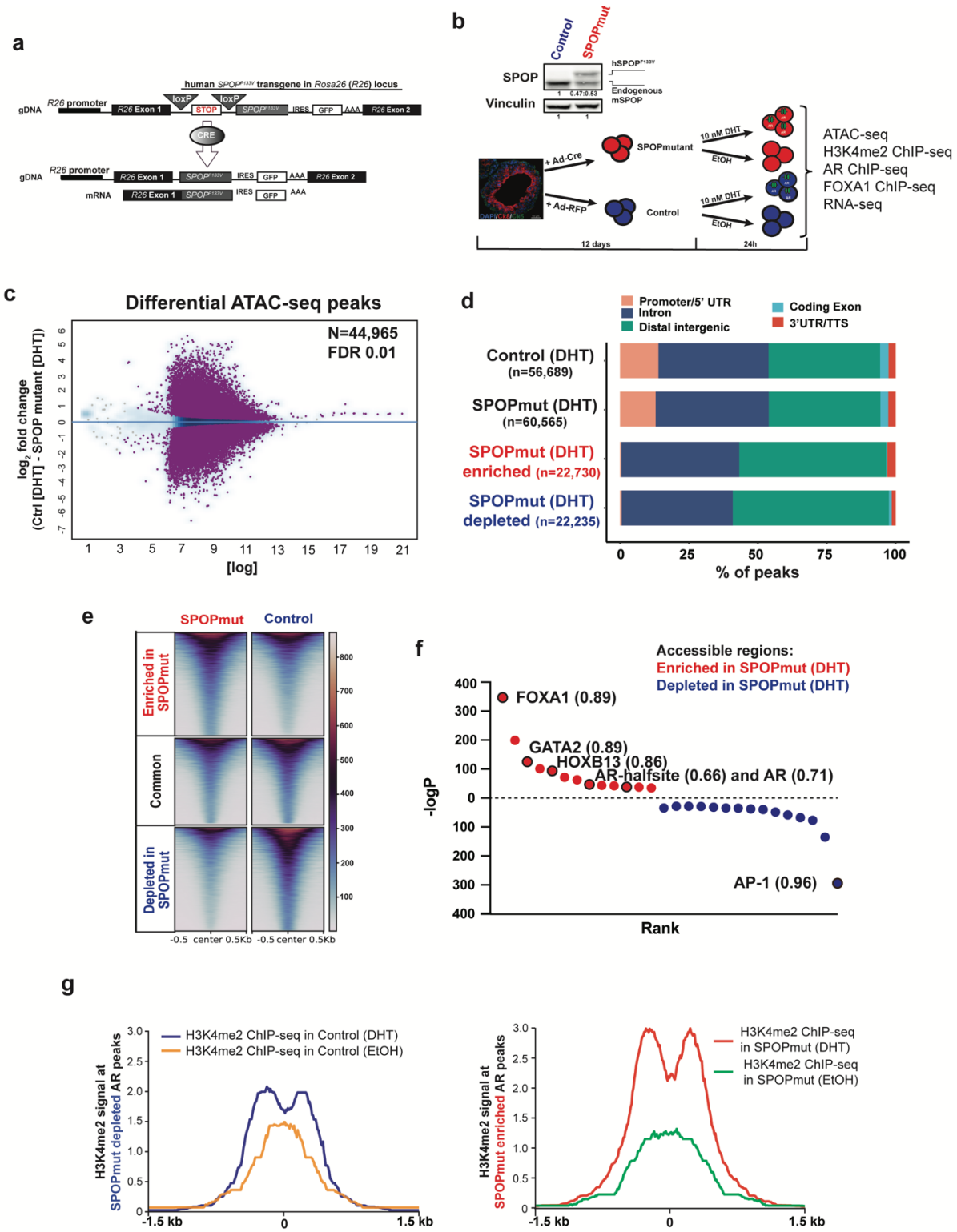

Fig. 2. Extensive remodelling of enhancers in SPOP-mut organoids. (a) Schematic of conditional *SPOP-F133V* construct in the *Rosa26* (*R26*) locus (top) and of the expressed transgenic

750 transcript after Cre introduction (bottom). **(b)** Illustration of the generation of the organoid lines
751 and treatments in addition to all the performed experiments. Up: Immunoblot showing
752 physiological levels of human SPOP-F133V (top band) in comparison to endogenous mouse SPOP
753 protein (bottom band). **(c)** Differential accessible peaks (purple) between Control (n=4) and SPOP-
754 mut (n=4) cells at FDR 0.01. **(d)** Genomic annotation of consensus and differential peaks showing
755 predominant enhancer location of *SPOP* mutant enriched and depleted accessible elements. **(e)**
756 Heatmap of accessible enhancers showing differential accessibility in SPOPmut enriched and
757 depleted peaks. **(f)** *De novo* motif analysis of SPOPmut enriched and depleted accessible DNA
758 regulatory regions. Enriched motifs are plotted according to their rank and *P* value. Values next to
759 the motif are the best match motif score (max. is 1). **(g)** H3K4me2 signal at the enhancers from
760 Control and *SPOP* mutant organoids with and without DHT stimulation at *SPOP* mutant depleted
761 AR peaks (left), and *SPOP* mutant enriched AR peaks (right).
762

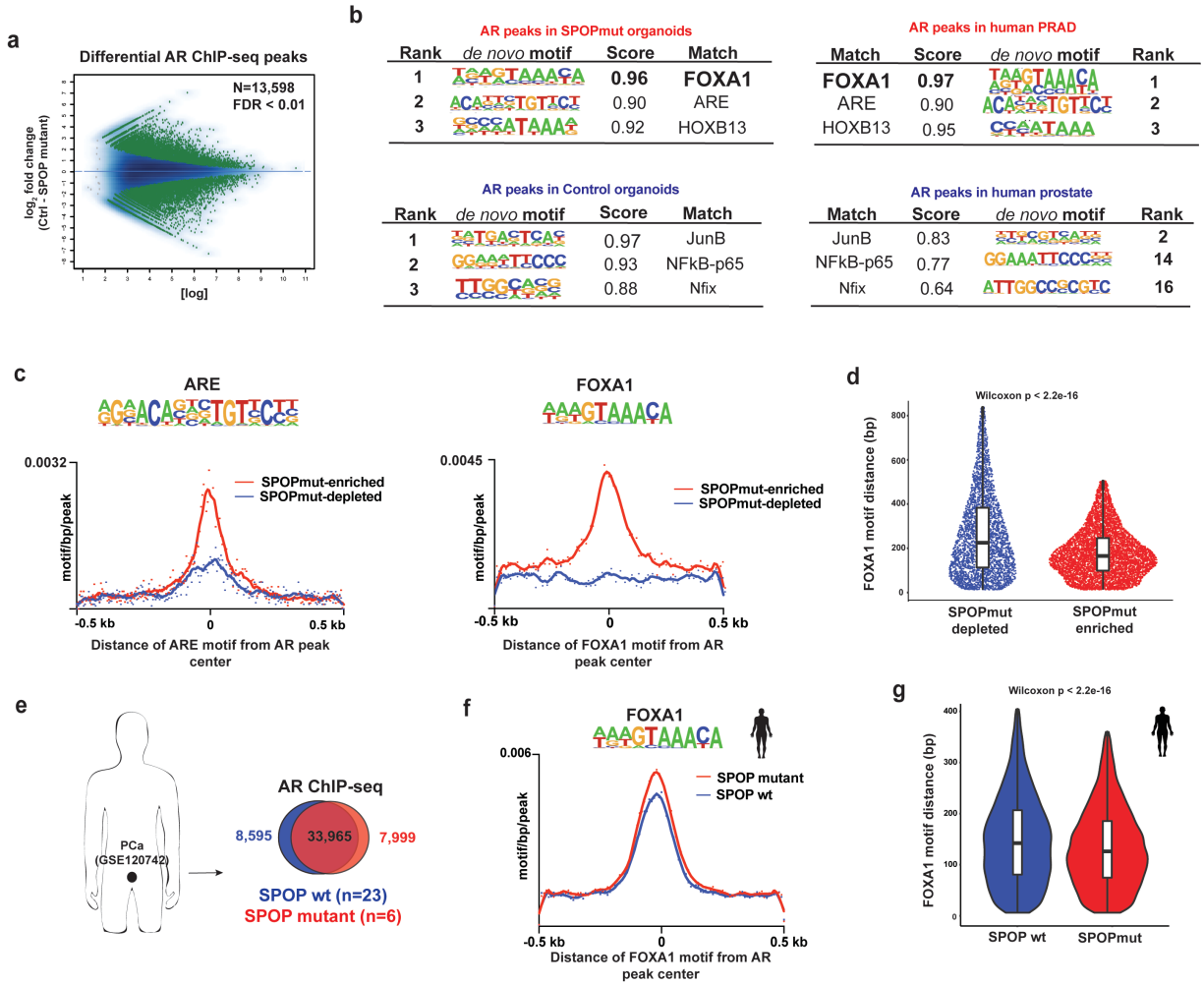

763

764 **Fig. 3. AR cistrome from *SPOP*-mutated cells is enriched for FOXA1 motifs. (a)** MA plot
765 showing AR differential sites (green dots) between Control and SPOP-F133V expressing
766 organoids using two biological replicates per condition. **(b)** *De novo* motif analysis of AR cistrome
767 in SPOPmut and Control organoids (right). Left: the same type of motif analysis performed on
768 human PRAD (Pomerantz et al., 2015). **(c)** Histograms of ARE (left) and FOXA1 (right) motif
769 densities within a 500 bp window around the center of each AR peak. Input files were from *SPOP*
770 mutant enriched (red line) and depleted (blue depleted) AR ChIP-seq peaks. **(d)** Sina plot –
771 distances of FOXA1 motif from the center of each AR peak. Input files were as in (c). **(e)** AR
772 ChIP-seq data from human prostate cancer tissues (Stelloo et al., 2018) (GSE120742). Peaks

773 coming from either PRAD with *SPOP* mutation or wt *SPOP* were merged and intersected. **(f)**
774 Histogram of FOXA1 motif density in AR binding sites from human prostate cells with SPOP-
775 F133V (red line) or wt SPOP (blue). **(g)** The distance of the FOXA1 motif from the center of AR
776 ChIP-seq peaks in each prostate cancer group.

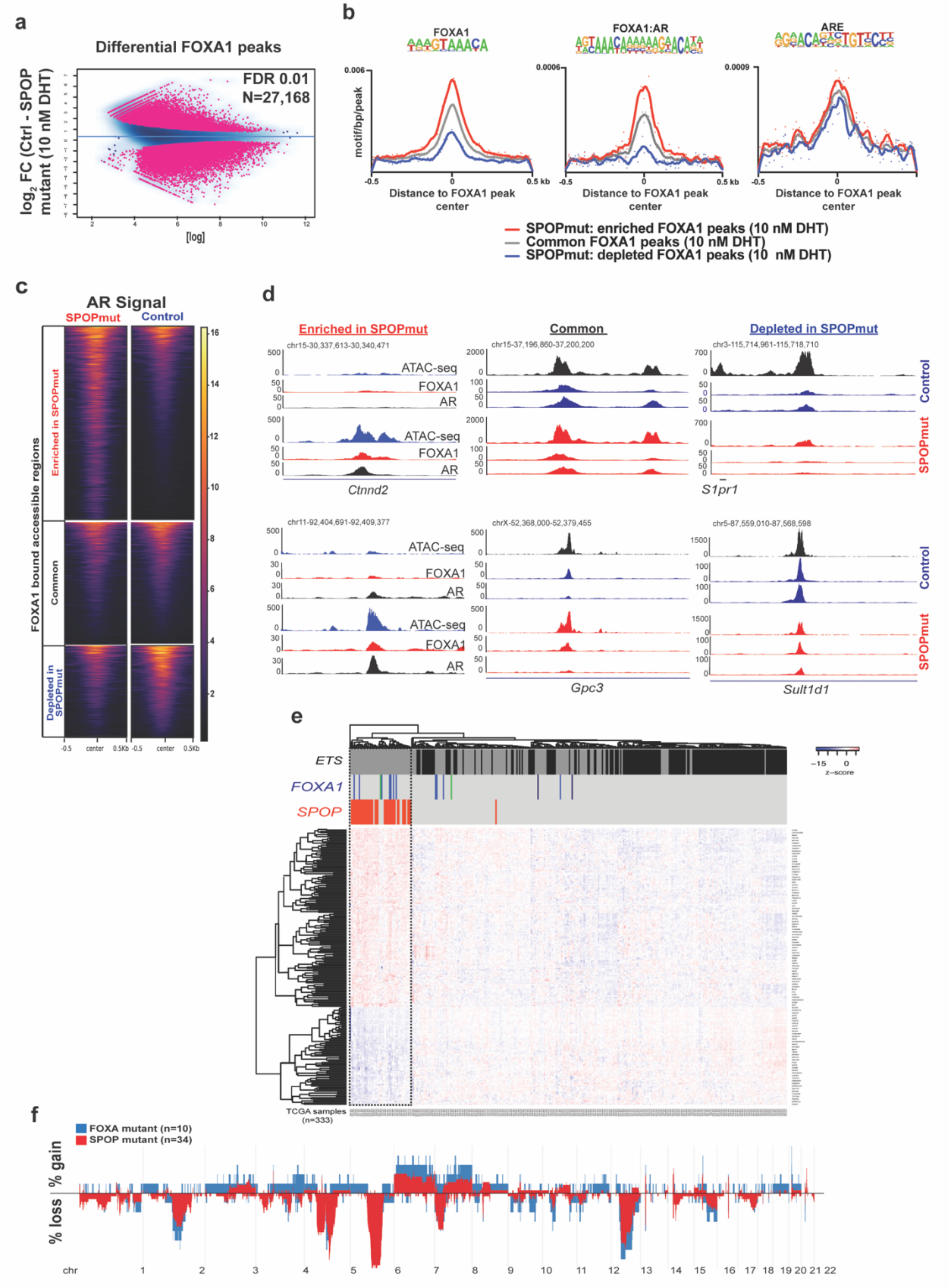
a
Differential FOXA1 peaks
FDR 0.01
N=27,168
log2 FC (Ctrl - SPOP mutant (10 nM DHT)
[log]
b
FOXA1
FOXA1:AR
ARE
motif/bp/peak
Distance to FOXA1 peak center
SPOPmut: enriched FOXA1 peaks (10 nM DHT)
Common FOXA1 peaks (10 nM DHT)
SPOPmut: depleted FOXA1 peaks (10 nM DHT)
c
AR Signal
SPOPmut
Control
FOXA1 bound accessible regions
Enriched in SPOPmut
Common
Depleted in SPOPmut
d
Enriched in SPOPmut
Common
Depleted in SPOPmut
ATAC-seq
FOXA1
AR
Control
SPOPmut
Ctnnd2
S1pr1
Gpc3
Sult1d1
e
ETS
FOXA1
SPOP
z-score
TCGA samples (n=333)
f
FOXA mutant (n=10)
SPOP mutant (n=34)
% gain
% loss
chr

778 **Fig. 4.** Increased binding of FOXA1 at *SPOP* mutant-specific AR sites. **(a)** Differential FOXA1
779 genome-wide binding in Control (n=2) and *SPOP* mutant (n=2) organoids upon AR activation. **(b)**
780 Motif densities within the center of FOXA1 peaks enriched (red) or depleted (blue) in *SPOP*
781 mutant murine organoids. Gray - The signal at regions where FOXA1 binding intensity does not
782 change. **(c)** AR binding signal at FOXA1-bound DNA regulatory elements that are common
783 between the lines or *SPOP* mutant enriched or depleted. (**d**) Representative Genome Browser
784 snapshots of regions analysed in (c). **(e, f)** Relationship between *SPOP*-mutant and *FOXA1*-mutant
785 subclasses of PRAD. **(e)** Classification of PRAD using the *SPOP*-mutant transcriptional classifier
786 (Liu et al., 2018). *FOXA1* mutations are depicted in blue (FKHD – DNA binding domain), green
787 (N-terminal domain) and black (truncations after FKHD domain). **(f)** Gene copy number profiles
788 of these molecular subclasses of PCa.
789

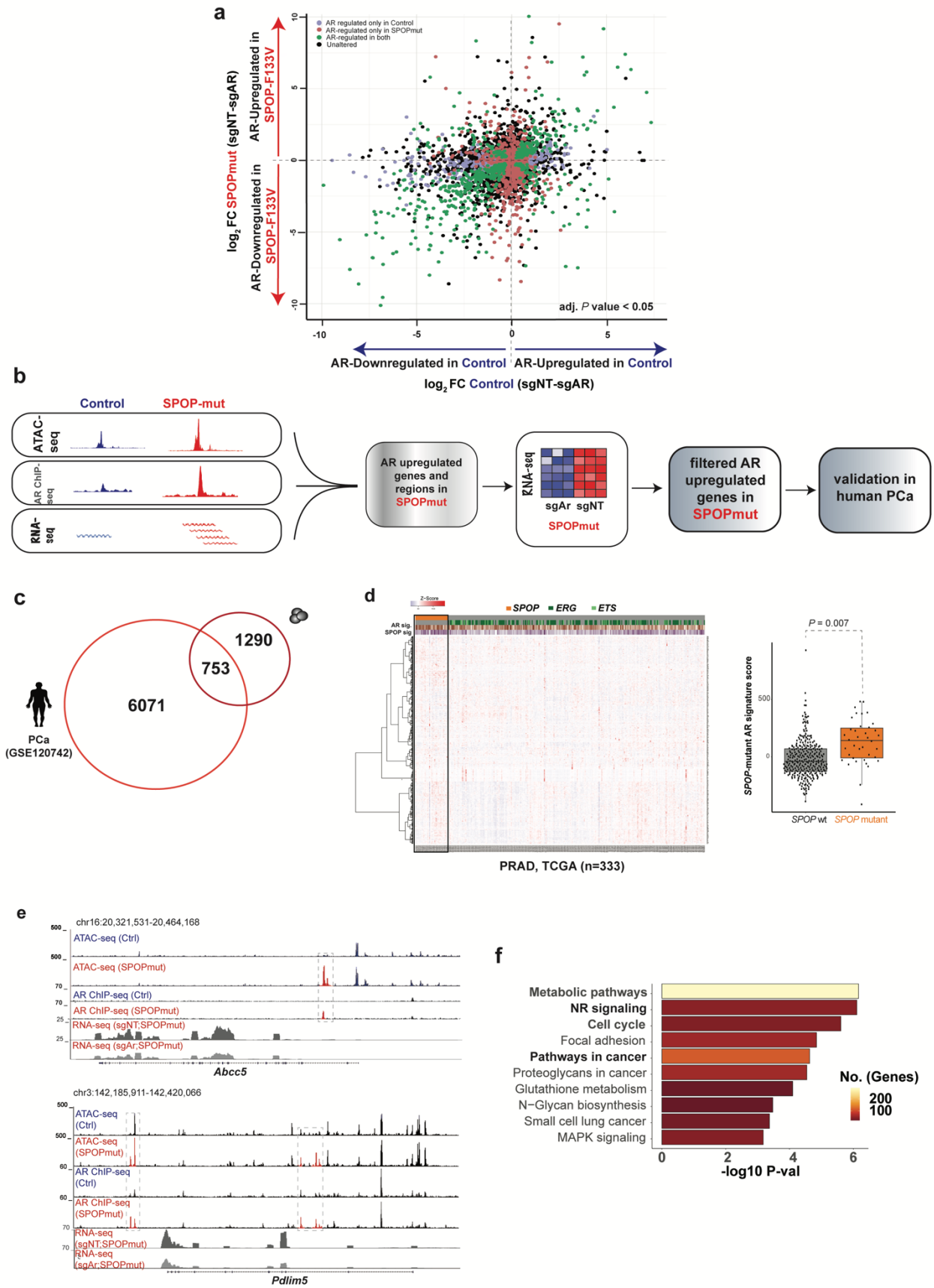
a
AR regulated only in Control
AR-regulated only in SPOPmut
AR-regulated in both
Unaltered
log2FC SPOPmut (sgNT-sgAR)
AR-Upregulated in SPOP-F133V
AR-Downregulated in SPOP-F133V
adj. P value < 0.05
AR-Downregulated in Control
AR-Upregulated in Control
log2FC Control (sgNT-sgAR)
b
Control
SPOP-mut
ATAC-seq
AR ChIP-seq
RNA-seq
AR upregulated genes and regions in SPOPmut
RNA-seq
sgAr sgNT
SPOPmut
filtered AR upregulated genes in SPOPmut
validation in human PCa
c
1290
753
6071
PCa (GSE120742)
d
SPOP
ERG
ETS
AR sig.
SPOP sig
PRAD, TCGA (n=333)
P = 0.007
SPOP-mutant AR signature score
SPOP wt
SPOP mutant
e
chr16:20,321,531-20,464,168
ATAC-seq (Ctrl)
ATAC-seq (SPOPmut)
AR ChIP-seq (Ctrl)
AR ChIP-seq (SPOPmut)
RNA-seq (sgNT;SPOPmut)
RNA-seq (sgAr;SPOPmut)
Abcc5
chr3:142,185,911-142,420,066
ATAC-seq (Ctrl)
ATAC-seq (SPOPmut)
AR ChIP-seq (Ctrl)
AR ChIP-seq (SPOPmut)
RNA-seq (sgNT;SPOPmut)
RNA-seq (sgAr;SPOPmut)
Pdlim5
f
Metabolic pathways
NR signaling
Cell cycle
Focal adhesion
Pathways in cancer
Proteoglycans in cancer
Glutathione metabolism
N−Glycan biosynthesis
Small cell lung cancer
MAPK signaling
No. (Genes)
200
100
-log10 P-val

790

791 **Fig. 5.** Nominating novel AR-regulated genes in the context of SPOP mutation **(a)** Plot showing
792 differentially expressed genes (adj. *P* value < 0.05) regulated by AR in Control cells (x-axis; blue)
793 and *SPOP*-mut cells (y-axis, red). **(b)** GSEA hallmark enrichment of AR-responsive genes in
794 Control (blue) and *SPOP* mutant (red) cells with plotted GSEA NES values. **(c)** Computational
795 steps to identify AR-upregulated genes specific to *SPOP* mutant human and murine cells. **(d)**
796 Overlapping AR-regulated genes in *SPOP*-mutant human PCa (Stelloo et al., 2018) and murine
797 cells. **(d)** Heatmap - Gene expression (n=753) in human PRAD samples (Cancer Genome Atlas
798 Research, 2015). Boxplots – PCa samples with higher expression of nominated genes (n=753)
799 have higher *SPOP*-mutant signature score. **(e)** Representative Genome Browser tracks of AR-
800 regulated regulatory regions and transcripts in *SPOP*-mut organoids. **(f)** Functional enrichment of
801 androgen-induced genes in murine *SPOP* mutant cells.
802

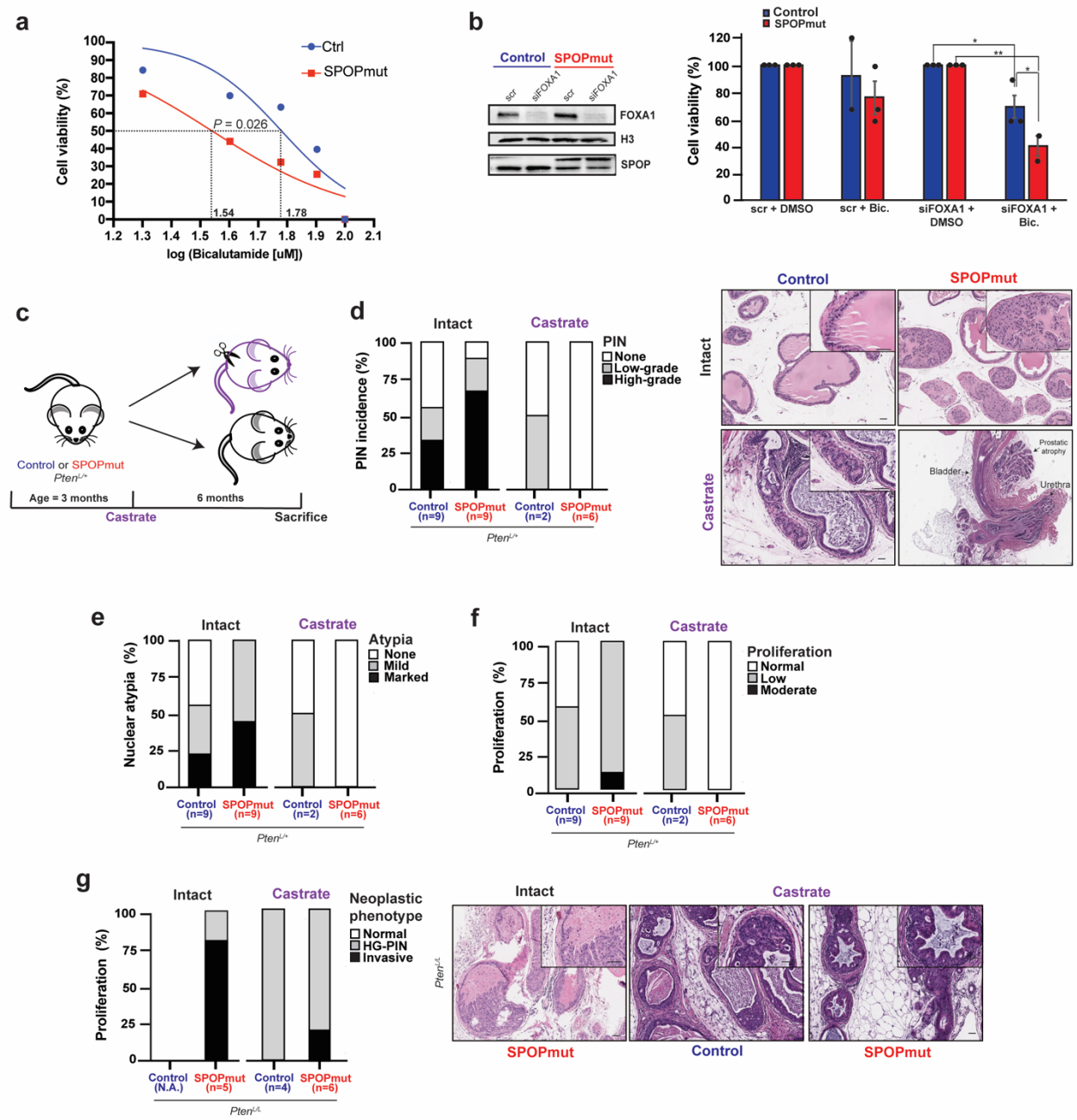

Fig. 6. The distinct phenotype of *SPOP* mutations shows dependency on functional AR signaling. **(a)** The dose-response curve (log scale) of Control and SPOPmut murine prostate organoids in response to bicalutamide. **(b)** Immunoblot of control and SPOPmut murine prostate cells after siRNA-mediated downregulation of FOXA1 (top) and cell viability of these cells after 20 μM bicalutamide treatment (bottom). **(c)** Schematic of castration experiment. **(d-f)** Incidence of PIN,

809 nuclear atypia and degree of proliferation in Control and SPOPmut mice before and after
810 castration. Representative H&E images are shown on the right and in Fig S5c-d. Scale bar, 50 mm.
811 **(g)** Incidence of neoplastic phenotypes (HG-PIN and invasive features such as necrosis, stromal
812 response and/or frank invasion) in Control and *SPOP-F133V* mice with representative images
813 shown on the right. Scale bar, 50 mm.

814

Figure 6

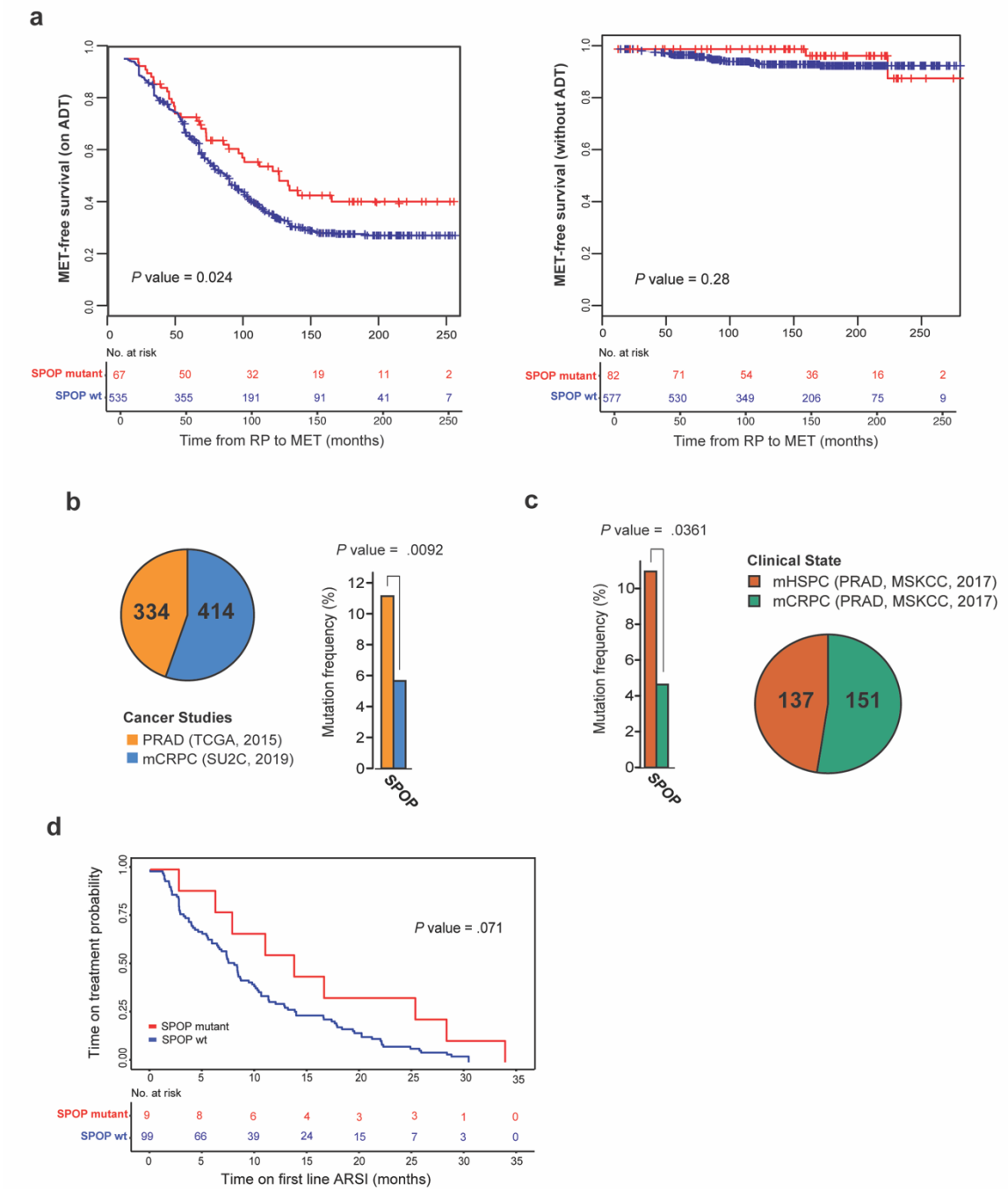

Fig. 7. Sensitivity of *SPOP* mutant PCa to therapies targeting AR signaling. **(a)** Significant clinical outcome difference between *SPOP* mutant and wild-type PCa via Kaplan-Meier analysis of metastasis (MET)-free survival for patients on androgen deprivation therapy (ADT) (left) or

819 without receiving ADT (right). **(b)** The occurrence of *SPOP* mutation in primary PCa (Cancer
820 Genome Atlas Research, 2015) and metastatic (mCRPC) samples (Abida et al., 2019). **(c)** When
821 metastatic prostate tumors (Abida et al., 2017) are compared – the hormone-sensitive ones
822 (mHSPC) have a higher frequency ($p < 0.0361$) of *SPOP* mutation than the resistant (mCRPC)
823 ones. **(d**) Kaplan-Meier analysis of *SPOP* wild-type and *SPOP*-mutated mCRPC tumors (27)
824 showing time on treatment with first-line androgen signaling inhibitors (ARSI).
825

826 **Supplementary Data**

827 Fig. S1. Distinct changes in androgen-induced chromatin and transcriptional landscape of normal
828 murine prostate cells.

829 Fig. S2. Androgen-dependent and independent chromatin remodelling of murine prostate cells
830 upon introduction of *SPOP* mutation.

831 Fig. S3. AR cistrome from *SPOP* mutant cells is enriched for FOXA1 and HOXB13 motifs.

832 Fig. S4. RNA-seq quality control.

833 Fig. S5. Murine SPOPmut prostate cells are more sensitive to anti-androgen treatment.

834 Table S3. Patient's characteristics from Decipher retrospective cohort.

835

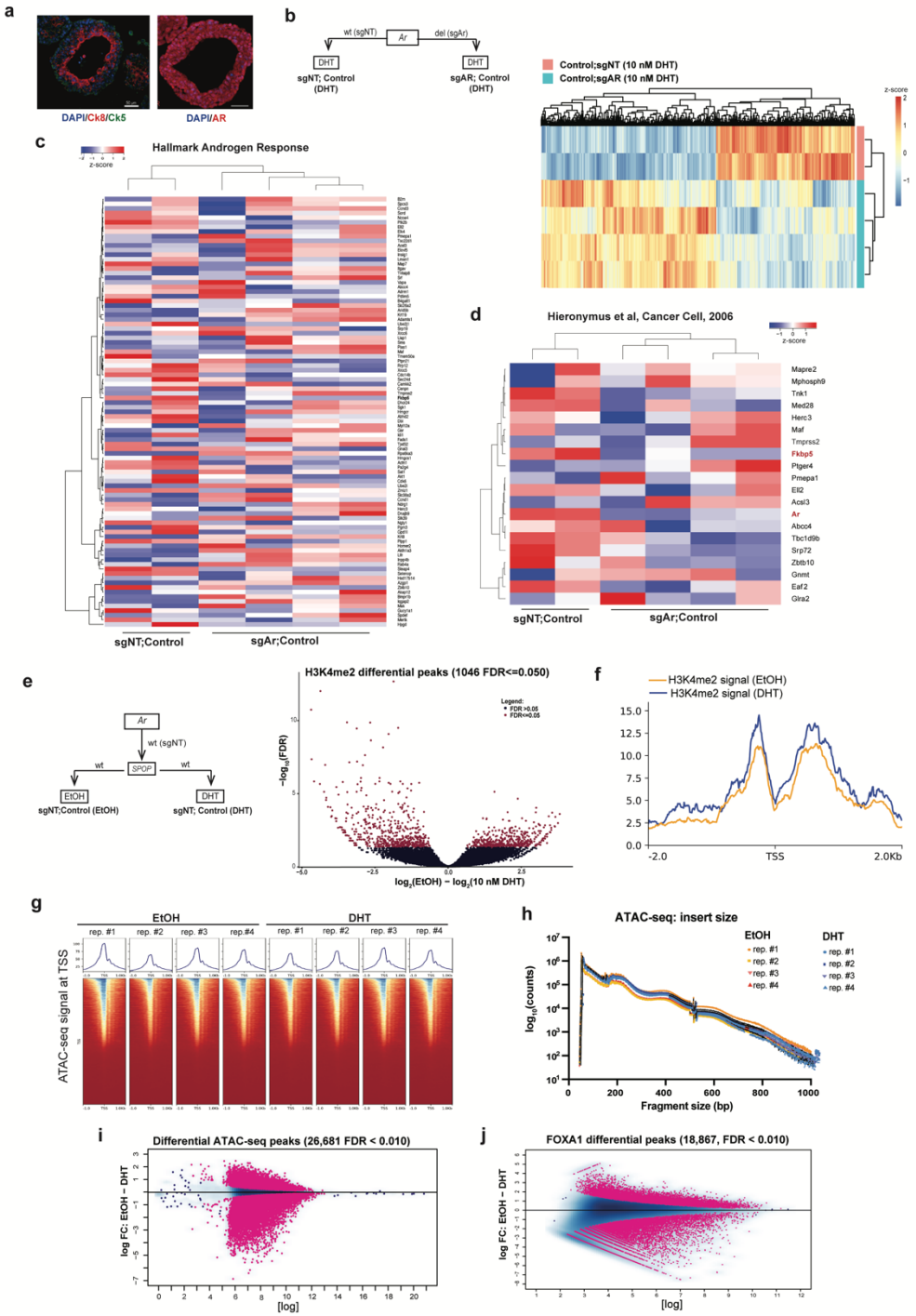

Fig. S1. Distinct changes in androgen-induced chromatin and transcriptional landscape of normal murine prostate cells (wildtype SPOP). **(a)** Morphology of murine prostate organoids (left: IF for Ck5 and Ck8) expressing AR (right). **(b)** Schematic representation of RNA-seq experiment and the heatmap showing all the differentially expressed genes. **(c, d)** Response of human AR-target

841 genes, from GSEA **(c)**, and literature (Hieronymus et al., 2006) **(d)**, to Ar downregulation in
842 normal murine prostate organoids. **(e)** Schematics of the ChIP-seq and ATAC-seq experiments
843 (left). Right – Volcano plot showing dynamics H3K4me2 ChIP-seq peaks at FDR 0.05. **(f)**
844 H3K4me2 signal at the promotors of the AR-upregulated genes in Control organoids (shown in
845 Figure 1c). **(g)** ATAC-seq quality metrics - distribution of DNA fragments in generated ATAC-
846 seq libraries. **(h)** ATAC-seq quality metrics – enrichment of ATAC-seq signal at the transcription
847 starts sites (TSS) of housekeeping genes. **(i)** Dynamic ATAC-seq peaks at FDR 0.01. **(j)** Dynamic
848 FOXA1 ChIP-seq peaks at FDR 0.01.
849

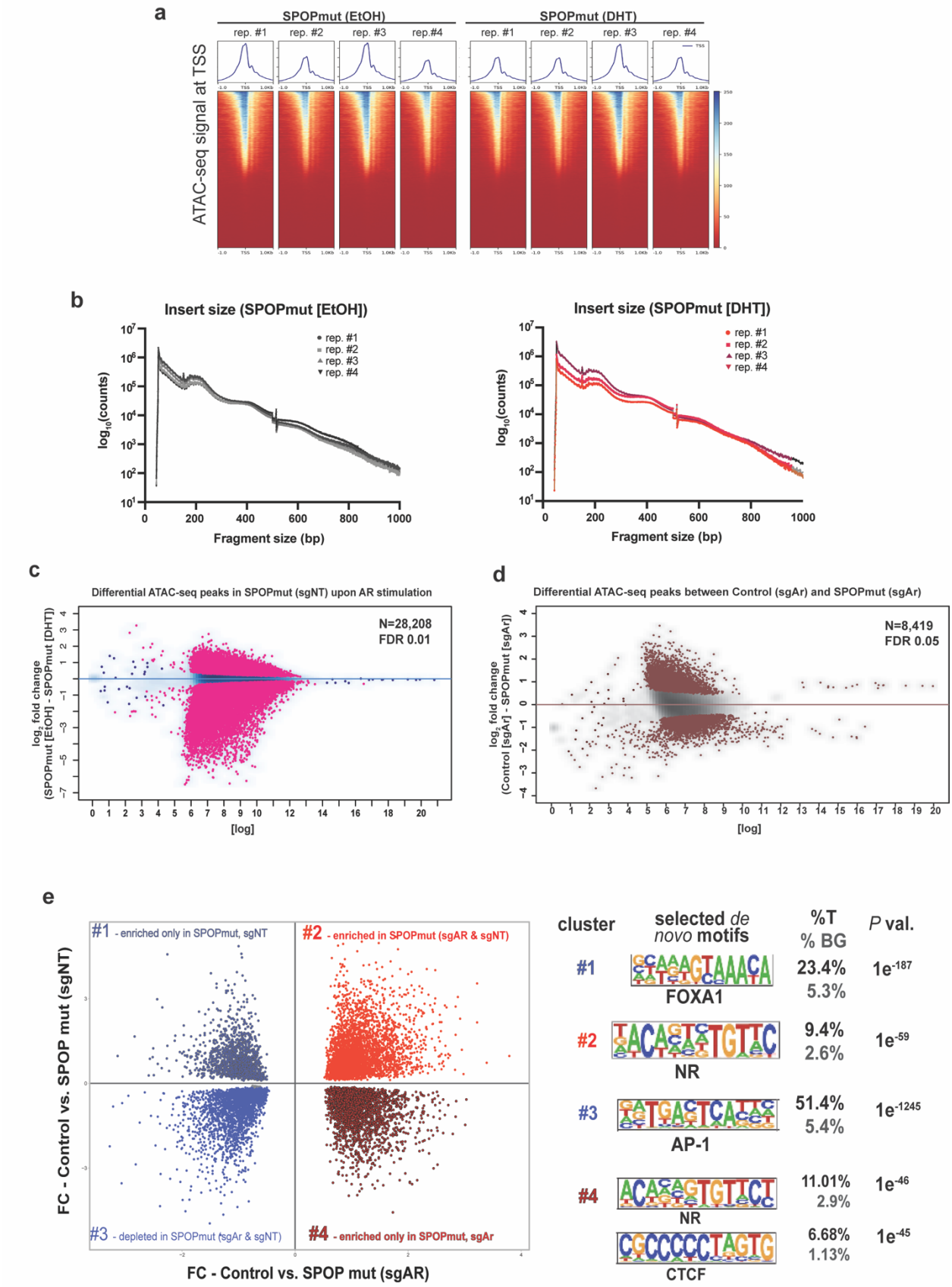
a
SPOPmut (EtOH)
SPOPmut (DHT)
rep. #1
rep. #2
rep. #3
rep.#4
ATAC-seq signal at TSS
b
Insert size (SPOPmut [EtOH])
Insert size (SPOPmut [DHT])
log10(counts)
Fragment size (bp)
c
Differential ATAC-seq peaks in SPOPmut (sgNT) upon AR stimulation
N=28,208
FDR 0.01
log2 fold change (SPOPmut [EtOH] - SPOPmut [DHT])
[log]
d
Differential ATAC-seq peaks between Control (sgAr) and SPOPmut (sgAr)
N=8,419
FDR 0.05
log2 fold change (Control [sgAr] - SPOPmut [sgAr])
[log]
e
#1 - enriched only in SPOPmut, sgNT
#2 - enriched in SPOPmut (sgAR & sgNT)
#3 - depleted in SPOPmut (sgAr & sgNT)
#4 - enriched only in SPOPmut, sgAr
FC - Control vs. SPOP mut (sgNT)
FC - Control vs. SPOP mut (sgAR)
cluster
selected de novo motifs
%T
% BG
P val.
#1
FOXA1
23.4%
5.3%
1e-187
#2
NR
9.4%
2.6%
1e-59
#3
AP-1
51.4%
5.4%
1e-1245
#4
NR
11.01%
2.9%
1e-46
CTCF
6.68%
1.13%
1e-45

850

851 **Fig. S2**. Androgen-dependent and independent chromatin remodeling of murine prostate cells
852 upon introduction of *SPOP* mutation. **(a, b)** Results of Encode quality metrics for ATAC-seq on
853 *SPOP* mutant cells (sgNT) before and after DHT treatment - enrichment at the promoters (i.e. TSS)
854 **(a)** and fragment size distribution **(b)**. **(c)** MA plot – dynamic accessible region upon AR
855 activation. **(d)** MA plot – dynamic regulatory regions induced by *SPOP* mutation when Ar is
856 downregulated. **(e)** Scatter plot – common and unique accessible regions in SPOP mutant cells
857 upon lower Ar expression. Right: results of de novo motif analysis. Black - target regions (%T).
858 Grey - background regions (%BG).
859

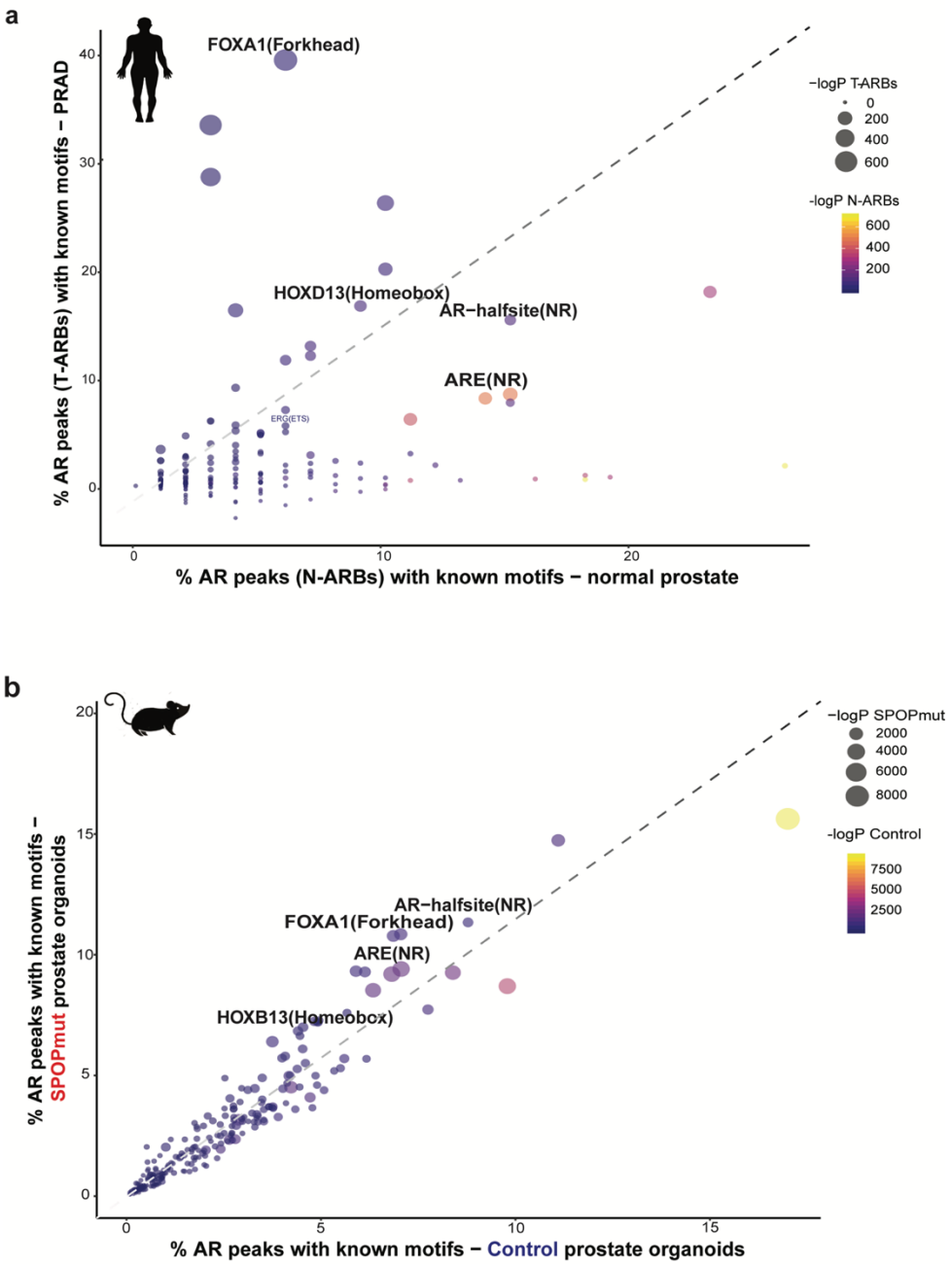

Fig. S3. AR cistrome from *SPOP* mutant cells is enriched for FOXA1 and HOXB13 motifs. **(a)** Comparison of the motifs found in AR peaks in normal human prostate tissues and cancers (Pomerantz et al., 2015). **(b)** Motifs found in AR bound regions in before and after introduction of SPOP mutation in normal murine prostate cells.

866

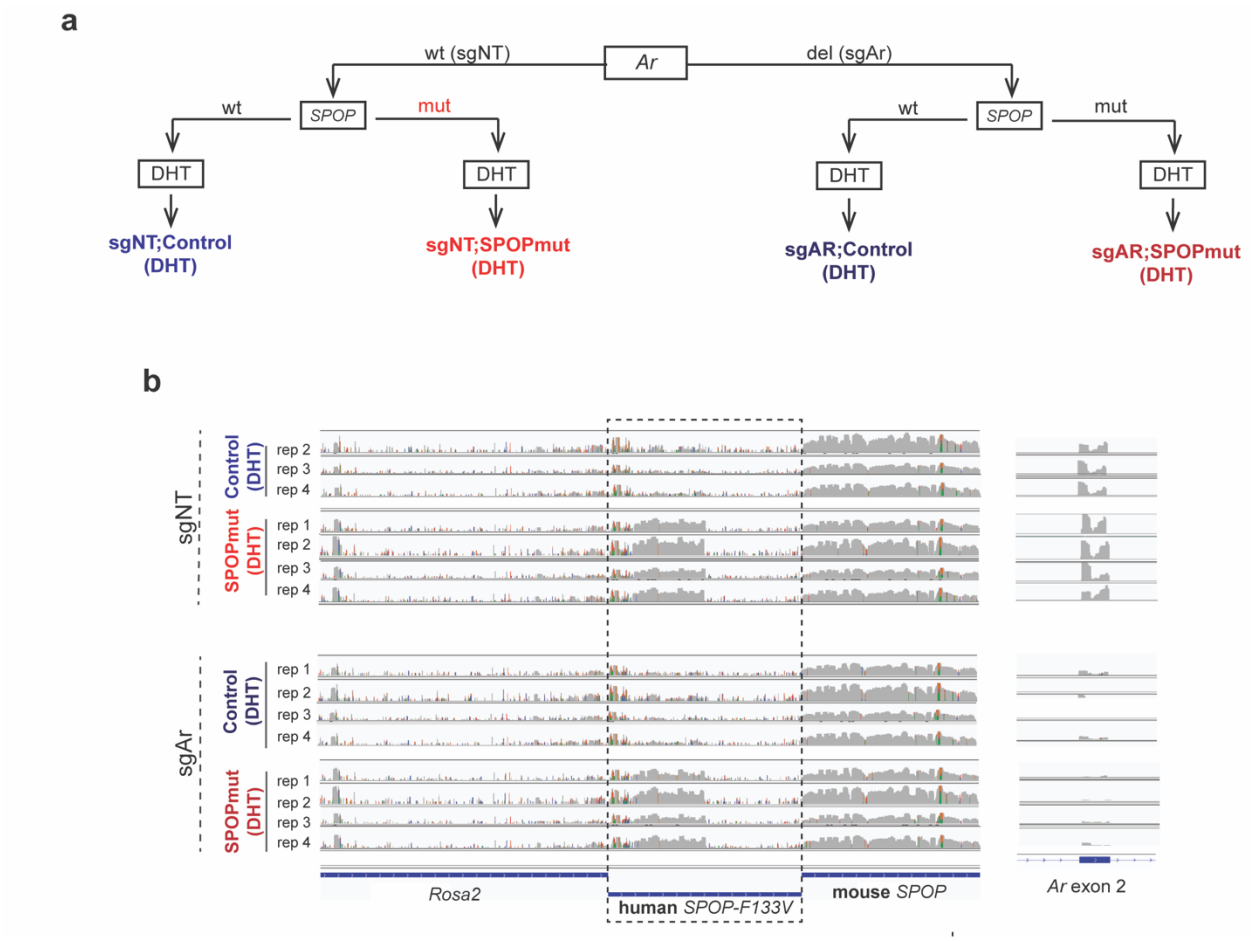

867

868 **Fig. S4.** RNA-seq quality control. **(a)** Schematic representation of all the generated RNA-seq

869 libraries. **(b)** Quality controls of the data – reads were aligned to human SPOP sequence (left)

870 and the Ar exon 2 (sgAr target).

871

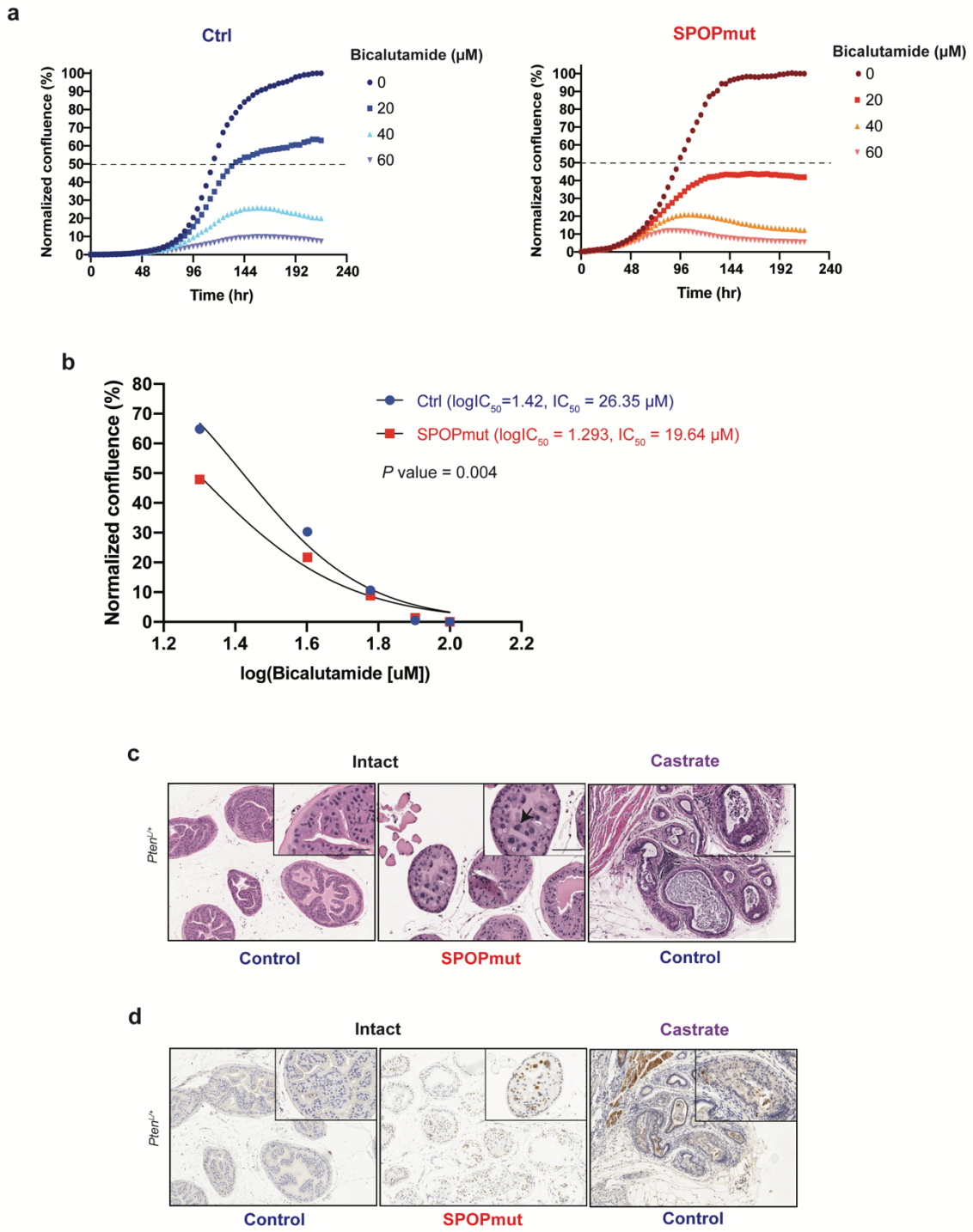

872

873 **Fig. S5.** Murine SPOPmut prostate cells show higher sensitivity to anti-androgen treatment. **(a,**

874 **b)** Slower proliferation of *SPOP*-mutant cells when treated with bicalutamide in 2D (a) and 3D

875 (b). **(c-d)** Representative images showing nuclear atypia and H&E staining.

Table S3. Patient's characteristics from Decipher retrospective cohort used for analysis in Fig.7a.

	SPOP mutant	*SPOP* wild-type
Cases	168	1,458
Median age (range)	65 (44-77)	62 (37-83)
Median PSA (range)	8.9 (1.9-87)	8.6 (0.1-201)
Gleason score (range)		
<=6	16	176
3+4	30	381
4+3	24	175
>=8	60	589
Pathological tumor stage		
pT2	66	464
pT3/4	82	722
Extracapsular extension	88 (53%)	855 (61%)
Lymp node invasion	20 (12%)	228 (16%)
Seminal vesicle invasion	35 (21%)	452 (32%)
Surgical margin	68 (41%)	703 (49%)

876